CMES, vol.23, no.3, pp.149-173, 2008

Boundary Element Method for an Inverse Problem in Magnetic Resonance Imaging Gradient Coils

Liviu Marin[1], **Henry Power**[1], **Richard W. Bowtell**[2], **Clemente Cobos Sanchez**[2], **Adib A. Becker**[1], **Paul Glover**[2] and **Arthur Jones**[1]

Abstract: We investigate the reconstruction of a divergence-free surface current distribution from knowledge of the magnetic flux density in a prescribed region of interest in the framework of static electromagnetism. This inverse problem is motivated by the design of gradient coils for use in magnetic resonance imaging (MRI) and is formulated using its corresponding integral representation according to potential theory. A novel boundary element method (BEM) which employs linear interpolation on quadratic surfaces and also satisfies the continuity equation for the current density, i.e. a divergence-free BEM, is presented. Since the discretised BEM system is ill-posed and hence the associated least-squares solution may be inaccurate and/or physically meaningless, the Tikhonov regularization method is employed in order to retrieve accurate and physically correct solutions.

Keyword: Inverse problem, regularization, divergence-free boundary element method, magnetic resonance imaging, electromagnetism, coil design.

1 Introduction

Magnetic resonance imaging (MRI) is a non-invasive technique for imaging the human body, which has revolutionised the field of diagnostic medicine. MRI relies on the generation of highly controlled magnetic fields that are essential to the process of image production. In particular, an extremely homogeneous, strong, static field is required to polarize the sample and provide a uniform frequency of precession, while pure field gradients are needed to encode the spatial origin of MR signals. The field gradients are generated by carefully arranged wire distributions generally placed on surfaces surrounding the imaging subject, known as gradient coils.

Over the last decades, many theoretical design methods for the construction of MRI gradient coils have been developed. In one of the first papers on this subject, Bangert and Mansfield (1982) produced a simple coil design that generated a high gradient strength per unit current whilst providing a low coil inductance. The majority of early MRI systems employed gradient coils based on simple saddle and loop units which are positioned so as to null as many undesired terms in the spherical harmonic expansion of the field at the coil centre, see e.g. Romeo and Hoult (1984). However, coils composed of discrete wire units generally have high inductance at fixed gradient strength and often have high length to diameter ratios. Improved performance can be achieved by using coils composed of distributed wirepaths which are spread more uniformly over the coil surface. In order to generate such designs, Turner (1986) developed a Fourier-Bessel expansion of the magnetic field generated by currents flowing on the surface of a cylinder. Inversion of the relationship between the current density and the corresponding magnetic field allowed the design of gradient, solenoidal and shim coils capable of generating a specified or target field. A method for designing coils with the minimum inductance consistent with the field specification was also presented by Turner (1988). Schweikert, Krieg and Noack (1988) have used a Lagrange

---

[1] School of Mechanical, Materials and Manufacturing Engineering, University of Nottingham, University Park, Nottingham NG7 2RD, UK.

[2] Sir Peter Mansfield Magnetic Resonance Centre, School of Physics and Astronomy, University of Nottingham, University Park, Nottingham NG7 2RD, UK.

multiplier formalism to allow the magnetic field specified at discrete locations in space to be used as constraints in an explicit minimisation of the power dissipated by a coil. Minimum power designs have also been proposed by Bowtell and Mansfield (1989). These methods of coil design have been implemented by using fast Fourier transforms to calculate the matrix elements and evaluate the current densities. The method of conjugate gradient descent for the minimisation of the gap functional between the desired and calculated magnetic fields with respect to the current element position has been addressed by Wong, Jesmanowicz and Hyde (1991). Carlson, Derby, Hawryszko and Weideman (1992) have developed an inductance minimisation technique which automatically incorporates finite length, by initially expanding the current density as a Fourier series. The majority of gradient coil designs are based on a cylindrical geometry in which the gradient wirepaths are confined to the surface of a cylinder. It is also, however, possible to design gradient coils using a variety of alternative geometries including planar and hemispherical forms, see Martens, Petropoulos, Brown, Andrews, Morich and Patrick (1991), and Green, Leggett and Bowtell (2005), respectively. Several generic gradient coil designs, as well as computational analysis approaches, were described in a review by Turner (1993).

There are important studies in the literature that are devoted to the design of gradient coils used in MRI based on computational methods. Liu (1998) has considered a bi-planar design and suggested a minimisation procedure for the magnetic energy, which is proportional to the total inductance, subject to the magnetic field being equal to a desired distribution in a specified region of interest. Green, Bowtell and Morris (2002) have proposed an approach similar to Liu (1998), namely the minimisation of a weighted combination of power, inductance and the squared difference between the actual and the desired fields. Leggett, Crozier, Blackband and Bowtell (2003) have investigated the multilayer transverse cylindrical coils by considering a cost function as a weighted combination of inductance and power loss, and imposing the condition that the magnetic field equals certain values at specified points. Recently, Lemdiasov and Ludwig (2005) have reported a new design approach for the construction of gradient coils used in MRI by considering an integral representation formula that satisfies the continuity equation for the surface current density, constant interpolation and the minimisation of a constrained cost function between the actual and the desired magnetic fields in a region of interest.

The boundary element method (BEM) is a numerical method essentially based on the integral formulation of the problem under consideration, see e.g. Brebbia, Telles and Wrobel (1984), and it is now a well established technique in computational electromagnetics and particularly in magnetostatics, see e.g. Adriaens, Delincé, Dular, Genon, Legros and Nicolet (1991), Nicolet, Dular, Genon and Legros (1992), and Nicolet (1991; 1994). To represent the current vector field over surfaces, it is important in a boundary integral formulation to express the current vector field with respect to an appropriate set of vector basis functions. The Rao-Wilton-Glisson (RWG) basis functions are the most used basis functions that preserve the continuity of the normal current vector across the interfaces between adjacent elements, see e.g. Rao, Wilton and Glisson (1982). Higher-order basis functions over triangular patches have been attempted by Wandzura (1992). However, no explicit and easy-to-implement formulations of the basis functions of general higher-order have been provided by Wandzura (1992). Popovic and Kolundzija (1994) have studied higher-order surface current basis functions using polynomials of parametric variables of the curved quadrilaterals and triangles with continuous normal component over the generalised quadrilaterals and triangles. Subsequently, this approach has been used by Andersen and Volakis (1999) to produce a higher-order tangential vector finite element basis in the Sobolev space $\mathscr{H}$(Curl) in 2D and 3D spaces, similar to the edge elements proposed by Nedelec (1980) and studied by Webb (1993). Cai (1999), Cai, Yu, Wang and Yu (2001), and

Cai, Yu and Yuan (2002) have developed a higher-order basis with the following properties (*i*) it is applicable to either curved or flat triangular and/or quadrilateral patches; (*ii*) it ensures the continuity of the normal components of the basis functions across common interfaces among adjacent patches; (*iii*) the usual RWG basis functions represent a particular case that corresponds to the lowest order approximation for the basis functions proposed by Cai (1999), Cai, Yu, Wang and Yu (2001), and Cai, Yu and Yuan (2002) over flat triangular patches.

Over the last two decades, both the BEM and the dual reciprocity BEM (DRBEM) have often been employed to solve inverse problems that occur in several branches of engineering and sciences, such as fluid flow [Lesnic, Elliott and Ingham (1997), Zeb, Ingham, Elliott and Lesnic (2000, 2002)], rock mechanics [Mustata, Harris, Elliott, Lesnic and Ingham (2000)], elasticity [Chao, Chen and Lin (2001), Marin, Elliott, Ingham and Lesnic (2001, 2002)], steady-state heat conduction [Lesnic, Elliott and Ingham (1997, 1998), Marin, Elliott, Heggs, Ingham, Lesnic and Wen (2003, 2004)], electrochemical processes [Noroozi, Sewell and Vinney (2006)], automatic inverse problem engine [de Lacerda and da Silva (2006)], etc.

The purpose of this paper is to investigate the numerical reconstruction of a divergence-free surface current distribution from knowledge of the magnetic flux density in a prescribed region of interest in the framework of static electromagnetism. This inverse problem is motivated by the design of gradient coils used in MRI and is formulated using its corresponding integral representation according to potential theory. In this study, a novel BEM which employs linear interpolation on quadratic surfaces and also satisfies the continuity equation for the current density, i.e. a divergence-free BEM, is developed. It should be mentioned that, in classical BEM formulations of the inverse problem analysed in this paper, the divergence-free condition for the current density has usually to be imposed in the form of additional constraints on the corresponding discretised BEM system of algebraic linear equations. However, in the present approach no additional constraints are required for the current density to satisfy the continuity equation, as the interpolation functions already satisfy this condition. Since the discretised BEM system is ill-posed and its associated solution obtained via a direct solver may be inaccurate and/or physically meaningless, regularization methods are employed in order to retrieve accurate and physically correct solutions. In our study, this is achieved by using the Tikhonov regularization method, where the regularization term is given by the norm related to the magnetic energy. The efficiency of the proposed numerical method is illustrated by numerical examples for cylindrical and hemispherical x− and z−gradient coil designs.

2 Mathematical formulation

In a non-magnetic material, such as biological tissue, the magnetic induction field $\mathbf{B} = \left(\mathrm{B_x}, \mathrm{B_y}, \mathrm{B_z}\right)^{\mathrm{T}}$ satisfies the following system of partial differential equations, see e.g. Jackson (1998):

$$\nabla \times \mathbf{B}(\mathbf{x}) = \mu_0 \mathbf{J}(\mathbf{x}), \quad \nabla \cdot \mathbf{B}(\mathbf{x}) = 0, \\ \mathbf{x} = (\mathrm{x}, \mathrm{y}, \mathrm{z}) \in \mathbb{R}^3. \tag{1}$$

Here $\mu_0 = 4\pi \times 10^{-7}\,\mathrm{N/A^2}$ is the permeability of the free-space and $\mathbf{J} = \left(\mathrm{J_x}, \mathrm{J_y}, \mathrm{J_z}\right)^{\mathrm{T}}$ is the current density which is defined as a surface current density $\mathbf{J}^{\mathrm{coil}} = \left(\mathrm{J_x}^{\mathrm{coil}}, \mathrm{J_y}^{\mathrm{coil}}, \mathrm{J_z}^{\mathrm{coil}}\right)^{\mathrm{T}}$, i.e.

$$\mathbf{J}(\mathbf{x}) = \mathbf{J}^{\mathrm{coil}}(\mathbf{x}')\,\delta\left(\mathbf{x}', \mathbf{x}\right), \quad \mathbf{x} \in \mathbb{R}^3, \quad \mathbf{x}' \in \Gamma_{\mathrm{coil}}, \tag{2}$$

where $\Gamma_{\mathrm{coil}} \subset \mathbb{R}^3$ is the coil surface and $\delta\left(\mathbf{x}', \mathbf{x}\right)$ is the Kronecker delta function, such that

$$\nabla \cdot \mathbf{J}^{\mathrm{coil}}(\mathbf{x}) = 0, \quad \mathbf{J}^{\mathrm{coil}}(\mathbf{x}) \cdot \nu(\mathbf{x}) = 0, \quad \mathbf{x} \in \Gamma_{\mathrm{coil}}, \tag{3}$$

with ν the outward unit vector normal to the coil surface Γ_{coil}.

If the vector potential $\mathbf{A} = \left(\mathrm{A_x}, \mathrm{A_y}, \mathrm{A_z}\right)^{\mathrm{T}}$ is introduced as:

$$\mathbf{B}(\mathbf{x}) = \nabla \times \mathbf{A}(\mathbf{x}), \quad \mathbf{x} \in \mathbb{R}^3, \tag{4}$$

then the system of partial differential equations (1) reduces to the following Poisson equation for the vector potential $\mathbf{A}$:

$$\nabla^2 \mathbf{A}(\mathbf{x}) = \mu_0 \mathbf{J}(\mathbf{x}), \quad \mathbf{x} \in \mathbb{R}^3. \tag{5}$$

In the *direct problem* formulation, the current density $\mathbf{J}^{\text{coil}}$ is known on the coil surface Γ_{coil}, satisfies the divergence-free condition (3_1) and lies on the plane tangent to the coil surface Γ_{coil}, see Eq. (3_2), whilst the vector potential $\mathbf{A}$ is determined from the Poisson equation (5) by employing its integral representation, namely

$$\begin{aligned}\mathbf{A}(\mathbf{x}) &= \mu_0 \int_{\mathbb{R}^3} \mathrm{u}^*\left(\mathbf{x},\mathbf{x}'\right) \mathbf{J}(\mathbf{x}')\,\mathrm{d}\mathbf{x}' \\ &= \mu_0 \int_{\Gamma_{\text{coil}}} \mathrm{u}^*\left(\mathbf{x},\mathbf{x}'\right) \mathbf{J}^{\text{coil}}(\mathbf{x}')\,\mathrm{d}\Gamma(\mathbf{x}'), \quad \mathbf{x} \in \mathbb{R}^3,\end{aligned} \tag{6}$$

where $\mathrm{u}^*(\mathbf{x},\mathbf{x}')$ is the Green function for the 3D Laplace equation given by

$$\mathrm{u}^*\left(\mathbf{x},\mathbf{x}'\right) = \frac{1}{4\pi|\mathbf{x}-\mathbf{x}'|}, \quad \mathbf{x},\mathbf{x}' \in \mathbb{R}^3. \tag{7}$$

On using Eqs. (4) and (6), the magnetic induction field may be recast as

$$\mathbf{B}(\mathbf{x}) = \mu_0 \int_{\Gamma_{\text{coil}}} \nabla_{\mathbf{x}} \mathrm{u}^*\left(\mathbf{x},\mathbf{x}'\right) \times \mathbf{J}^{\text{coil}}(\mathbf{x}')\,\mathrm{d}\Gamma(\mathbf{x}'), \quad \mathbf{x} \in \mathbb{R}^3. \tag{8}$$

Motivated by the design of gradient coils for use in MRI, we investigate the reconstruction of the divergence-free surface current distribution $\mathbf{J}^{\text{coil}}$ from knowledge of one component of the magnetic flux density $\mathbf{B}$, generally B_z, in a prescribed region of interest $\Omega \subset \mathbb{R}^3$. More precisely, we focus on the following *inverse problem*:

Given $\widetilde{\mathrm{B}}_z(\mathbf{x}), \mathbf{x} \in \Omega$, find $\mathbf{J}^{\text{coil}}(\mathbf{x}), \mathbf{x} \in \Gamma_{\text{coil}}$, such that:

$$\begin{cases}\mathrm{B}_z(\mathbf{x}) = \widetilde{\mathrm{B}}_z(\mathbf{x}), & \mathbf{x} \in \Omega, \\ \nabla \cdot \mathbf{J}^{\text{coil}}(\mathbf{x}) = 0, \mathbf{J}^{\text{coil}}(\mathbf{x}) \cdot \nu(\mathbf{x}) = 0, & \mathbf{x} \in \Gamma_{\text{coil}}.\end{cases} \tag{9}$$

3 Divergence-free BEM

In this section, we generalise the approach of Lemdiasov and Ludwig (2005) which is based on the integral representation formula for the vector potential that satisfies the continuity equation for the surface current density and employs a constant approximation for the field variables corresponding to linear (flat) elements. More specifically, starting from the integral representation (6) for the vector potential $\mathbf{A}$, we develop a linear interpolation for the current density $\mathbf{J}^{\text{coil}}$ which ensures that the current density is divergent-free, i.e. the continuity equation (3_1) is satisfied, and that it also lies in the plane tangential to the coil surface Γ_{coil}, see Eq. (3_2).

3.1 Geometry of the boundary elements

Assume that the coil surface Γ_{coil} is approximated as $\Gamma_{\text{coil}} \approx \bigcup_{\mathrm{n}=1}^{\mathrm{N}} \Gamma_{\mathrm{n}}$, where Γ_{n}, $1 \le \mathrm{n} \le \mathrm{N}$, are triangular boundary elements (not necessarily flat). In the subsequent analysis, we use the following notation, see also Fig. 1:

- $\Gamma_{\mathrm{n}} := \triangle \mathbf{x}^{\mathrm{n}1}\mathbf{x}^{\mathrm{n}2}\mathbf{x}^{\mathrm{n}3}$, $1 \le \mathrm{n} \le \mathrm{N}$, triangular boundary elements;
- $\mathbf{x}^{\mathrm{nj}}$, $1 \le \mathrm{j} \le \mathrm{N_e}$, local nodes corresponding to the triangular boundary element Γ_{n}, e.g. $\mathrm{N_e} = 3$ and $\mathrm{N_e} = 6$ in the case of linear and quadratic triangular boundary elements, respectively;
- The first three local nodes, i.e. $\mathbf{x}^{\mathrm{nj}}$, $1 \le \mathrm{j} \le 3$, correspond to the vertices of the triangular boundary element Γ_{n};
- Γ_{nj} the edge of the triangular boundary element Γ_{n} opposite to the vertex $\mathbf{x}^{\mathrm{nj}}$, $1 \le \mathrm{j} \le 3$;
- ν^{nj} the outward unit vector normal to the edge Γ_{nj}, $1 \le \mathrm{j} \le 3$, lying in the plane tangential to the triangular boundary element Γ_{n};
- ν^{n} the outward unit vector normal to the triangular boundary element Γ_{n};
- $\mathbf{x}^{\mathrm{m}}$, $1 \le \mathrm{m} \le \mathrm{M}$, global nodes on the coil surface Γ_{coil} corresponding to the BEM mesh

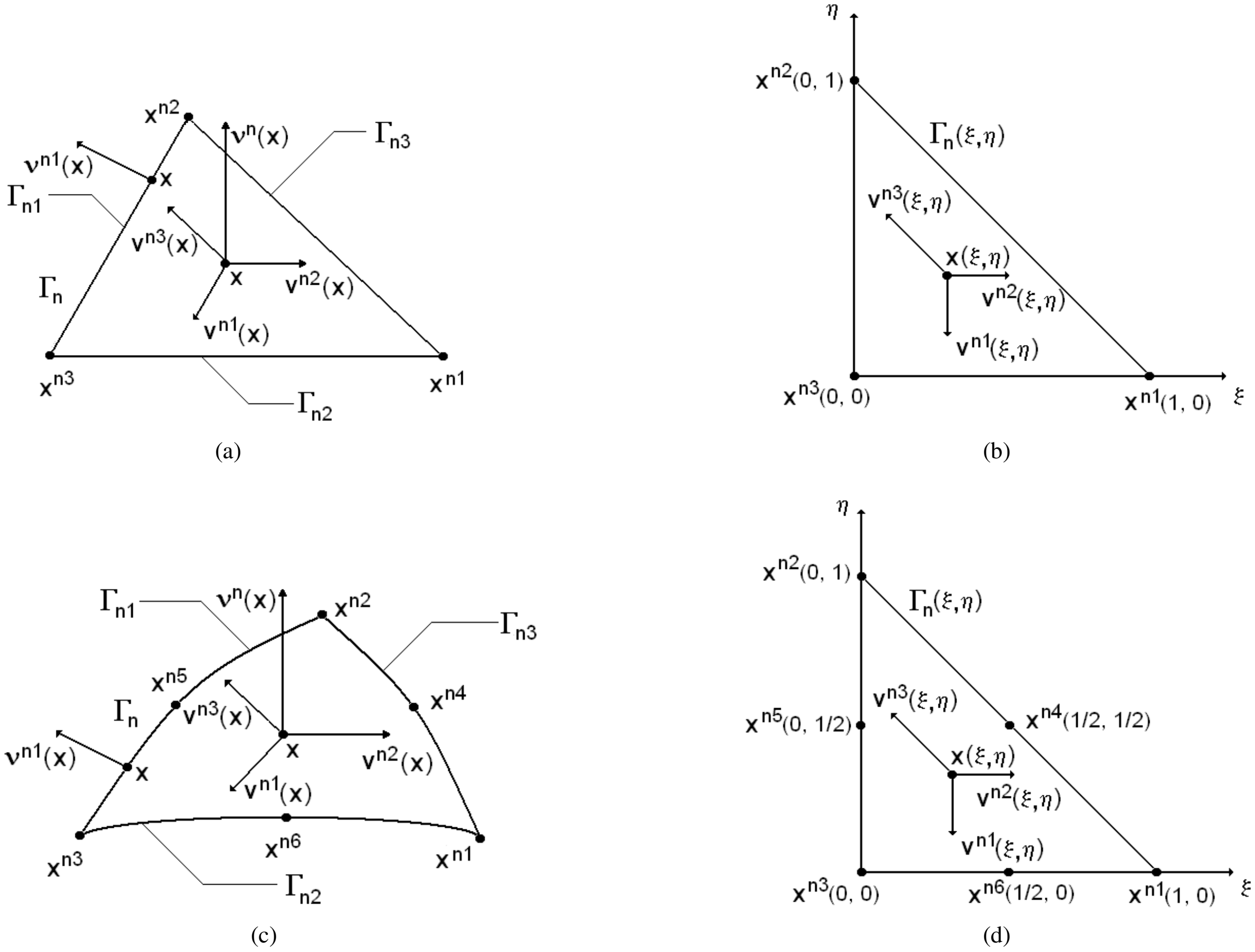

Figure 1: Schematic diagram of the (a) linear and (c) quadratic triangular boundary elements Γ_{n} in the physical space $\mathbb{R}^3$. Schematic diagram of the transformed (b) linear and (d) quadratic triangular boundary elements $\Gamma_{\mathrm{n}}(\xi,\eta)$ in the parametric space (ξ,η).

generated by the triangular boundary elements Γ_{n}, $1 \le \mathrm{n} \le \mathrm{N}$. Note that every global node is a vertex of at least one triangular boundary element;

- N the number of triangular boundary elements;
- M the number of global nodes on the coil surface Γ_{coil};
- $\mathrm{N_e}$ the number of local nodes corresponding to each triangular boundary element Γ_{n}.

The parametrization of the triangular boundary elements is given by

$$(\xi,\eta) \in \Gamma_{\mathrm{n}}(\xi,\eta) \longmapsto \mathbf{x}(\xi,\eta) \in \Gamma_{\mathrm{n}}$$
$$\mathbf{x}(\xi,\eta) = \sum_{\mathrm{j}=1}^{\mathrm{N_e}} \mathrm{N_j}(\xi,\eta)\,\mathbf{x}^{\mathrm{nj}}, \tag{10}$$

where

$$\Gamma_{\mathrm{n}}(\xi,\eta) = \left\{ (\xi,\eta) \,|\, \xi \ge 0, \eta \ge 0, \xi+\eta \le 1 \right\}$$

and $\mathrm{N_j}(\xi,\eta)$, $1 \le \mathrm{j} \le \mathrm{N_e}$, are geometrical shape functions which, for the sake of completeness, are presented in Appendix A. Consequently, the derivatives in the $\xi-$ and $\eta-$directions may be recast as:

$$\begin{cases} \tau^{n\xi}(\xi,\eta) = \frac{\partial \mathbf{x}(\xi,\eta)}{\partial \xi} = \sum\limits_{j=1}^{N_e} \dfrac{\partial N_j(\xi,\eta)}{\partial \xi} \mathbf{x}^{nj} \\ \tau^{n\eta}(\xi,\eta) = \frac{\partial \mathbf{x}(\xi,\eta)}{\partial \eta} = \sum\limits_{j=1}^{N_e} \dfrac{\partial N_j(\xi,\eta)}{\partial \eta} \mathbf{x}^{nj}. \end{cases} \tag{11}$$

Then the surface metric (Jacobian) J^n and the outward unit vector ν^n normal to the triangular boundary element Γ_n are given by:

$$J^n(\xi,\eta) = |\tau^{n\xi}(\xi,\eta) \times \tau^{n\eta}(\xi,\eta)| \tag{12}$$

and

$$\nu^n(\xi,\eta) = \frac{1}{J^n(\xi,\eta)} \tau^{n\xi}(\xi,\eta) \times \tau^{n\eta}(\xi,\eta) \tag{13}$$

respectively.

3.2 Basis functions

On every triangular boundary element Γ_n, we define the following vectors, as shown in Fig. 1:

$$\begin{cases} \mathbf{v}^{n1}(\xi,\eta) = -\dfrac{1}{J^n(\xi,\eta)} \tau^{n\eta}(\xi,\eta) \\ \mathbf{v}^{n2}(\xi,\eta) = \dfrac{1}{J^n(\xi,\eta)} \tau^{n\xi}(\xi,\eta) \\ \mathbf{v}^{n3}(\xi,\eta) = \dfrac{1}{J^n(\xi,\eta)} \left[-\tau^{n\xi}(\xi,\eta) + \tau^{n\eta}(\xi,\eta) \right]. \end{cases} \tag{14}$$

From definition (14), it follows that the vectors $\mathbf{v}^{nj}(\xi,\eta)$ satisfy the identity:

$$\sum_{j=1}^{3} \mathbf{v}^{nj}(\xi,\eta) = 0 \text{ for } \mathbf{x} = \mathbf{x}(\xi,\eta) \in \Gamma_n. \tag{15}$$

Next, we define the incidence function i as follows:

$$\begin{aligned} &i(\cdot,\cdot) : \{1,2,\ldots,M\} \times \{1,2,\ldots,N\} \longrightarrow \{0,1,2,3\} \\ &(m,n) \longmapsto \\ &i(m,n) = \begin{cases} 0 & \text{if } \mathbf{x}^m \neq \mathbf{x}^{nj}, \ \forall j \in \{1,2,3\} \\ j & \text{if } \exists j \in \{1,2,3\} : \mathbf{x}^m = \mathbf{x}^{nj}. \end{cases} \end{aligned} \tag{16}$$

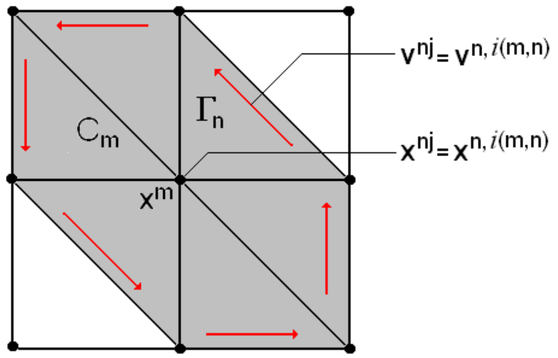

Figure 2: The set C_m of boundary elements Γ_n adjacent to the global node $\mathbf{x}^m$ and the corresponding vector $\mathbf{v}^{n,i(m,n)}(\mathbf{x})$ in the physical space $\mathbb{R}^3$.

For every global node $\mathbf{x}^m$, $1 \leq m \leq M$, we define the set $C_m \subset \Gamma_{coil}$ of triangular boundary elements Γ_n, $1 \leq n \leq N$, adjacent to $\mathbf{x}^m$, see also Fig. 2, i.e.

$$C_m = \bigcup_{\substack{n=1 \\ i(m,n) \neq 0}}^{N} \Gamma_n, \quad 1 \leq m \leq M. \tag{17}$$

The vector basis function $\mathbf{f}^m$ associated with the global node $\mathbf{x}^m$ is defined by

$$\begin{aligned} &\mathbf{f}^m(\cdot) : \Gamma_{coil} \longrightarrow \mathbb{R}^3 \\ &\mathbf{f}^m(\mathbf{x}) = \begin{cases} \mathbf{v}^{n,i(m,n)}(\mathbf{x}) & \text{if } \mathbf{x} \in C_m \\ \mathbf{0} & \text{if } \mathbf{x} \notin C_m \end{cases} \end{aligned} \tag{18}$$

and clearly its support is a subset of C_m, i.e. $\operatorname{supp} \mathbf{f}^m = \{ \mathbf{x} \in \Gamma_{coil} \, | \, \mathbf{f}^m(\mathbf{x}) \neq \mathbf{0} \} \subset C_m$.

3.3 Surface current density

The current density $\mathbf{J}^{coil}$ on the coil surface Γ_{coil} is then approximated by

$$\begin{aligned} \mathbf{J}^{coil}(\mathbf{x}) &\approx \sum\nolimits_{m=1}^{M} I_m \mathbf{f}^m(\mathbf{x}) \\ &= \sum\nolimits_{m=1}^{M} I_m \sum\nolimits_{\substack{n=1 \\ i(m,n) \neq 0}}^{N} \mathbf{v}^{n,i(m,n)}(\mathbf{x}), \ \mathbf{x} \in \Gamma_{coil}, \end{aligned} \tag{19}$$

where $I_m \in \mathbb{R}$, $1 \leq m \leq M$, are unknown coefficients that correspond to the stream function intensities at each of the global nodes $\mathbf{x}^m$, $1 \leq m \leq M$, see also Lemdiasov and Ludwig (2005). For direct problems, the stream function intensities are determined from appropriate boundary conditions, while in the case of inverse problems, they are obtained by solving a minimisation problem.

It should be noted that the degree of the approximation (19) for the surface current density $\mathbf{J}^{\mathrm{coil}}$ is one degree less than the degree of the triangular boundary elements Γ_{n}, $1 \leq \mathrm{n} \leq \mathrm{N}$, since the vectors $\mathbf{v}^{\mathrm{nj}}(\xi,\eta)$, $1 \leq \mathrm{j} \leq 3$, are related to the derivatives of the geometrical shape functions $\mathrm{N}_{\mathrm{j}}(\xi,\eta)$, $1 \leq \mathrm{j} \leq \mathrm{N}_{\mathrm{e}}$, associated with the triangular boundary element Γ_{n}, see Eqs. (10) – (14). More precisely, linear and quadratic triangular boundary elements provide constant and linear approximations for the surface current density, respectively. It is important to note that the collocation points, i.e. global nodes, are always located at the vertices of the triangular boundary elements employed in the BEM meshing of the coil surface, Γ_{coil}. Therefore, increasing the degree of interpolation of the surface current density does not affect the number of collocation points and hence the dimension of the resulting BEM system of linear algebraic equations. From Eqs. (13) and (14) it follows that for every triangular boundary element Γ_{n} the vectors $\mathbf{v}^{\mathrm{nj}}(\xi,\eta)$, $1 \leq \mathrm{j} \leq 3$, and the outward unit normal vector $\nu^{\mathrm{n}}(\xi,\eta)$ are orthogonal and hence expression (19) forces the approximated current density $\mathbf{J}^{\mathrm{coil}}$ to lie in the plane tangential to the coil surface, Γ_{coil}, i.e. condition (3_2) is satisfied. Furthermore, the interpolation given by Eq. (19) is divergence-free pointwise, i.e. the divergence-free condition (3_1) is satisfied for both types of triangular elements considered, namely linear and quadratic triangular boundary elements. In the case of linear triangular elements, the divergence-free condition is clearly satisfied since the basis vectors given by Eq. (14) are constant over each triangular element. Although not so evident, it can easily be shown that the same divergence-free property is always preserved for linear interpolation over quadratic triangular elements, as shown in Appendix B by considering a local spherical coordinates for quadratic triangular boundary elements.

The unknown coefficients I_{m}, $1 \leq \mathrm{m} \leq \mathrm{M}$, can also be defined locally for every triangular boundary element Γ_{n}, $1 \leq \mathrm{n} \leq \mathrm{N}$, i.e.

$$\mathrm{I}_{\mathrm{nj}} = \mathrm{I}_{\mathrm{m_j}}, \text{ where } \mathrm{m_j} \in \{1,2,\ldots,\mathrm{M}\}: \, i\left(\mathrm{m_j},\mathrm{n}\right) = \mathrm{j}. \tag{20}$$

Consequently, we obtain the local approximation on every triangular boundary element Γ_{n}, $1 \leq \mathrm{n} \leq \mathrm{N}$,

$$\mathbf{J}^{\mathrm{coil}}(\mathbf{x}) \approx \sum_{\mathrm{j}=1}^{3} \mathrm{I}_{\mathrm{nj}}\, \mathbf{v}^{\mathrm{nj}}(\mathbf{x}) = \sum_{\mathrm{j}=1}^{3} \mathrm{I}_{\mathrm{m_j}}\, \mathbf{v}^{\mathrm{n},i(\mathrm{m_j},\mathrm{n})}(\mathbf{x}), \quad \mathbf{x} \in \Gamma_{\mathrm{n}}. \tag{21}$$

3.4 Magnetic vector potential

According to Eqs. (6), (19) and (21), the magnetic vector potential $\mathbf{A}$ is approximated by

$$\mathbf{A}(\mathbf{x}) \approx \frac{\mu_0}{4\pi} \sum_{\mathrm{n}=1}^{\mathrm{N}} \int_{\Gamma_{\mathrm{n}}} \sum_{\mathrm{j}=1}^{3} \mathrm{I}_{\mathrm{nj}} \frac{\mathbf{v}^{\mathrm{nj}}(\mathbf{x}')}{|\mathbf{x}-\mathbf{x}'|}\, \mathrm{d}\Gamma(\mathbf{x}')$$

$$= \frac{\mu_0}{4\pi} \sum_{\mathrm{m}=1}^{\mathrm{M}} \mathrm{I}_{\mathrm{m}} \sum_{\substack{\mathrm{n}=1 \\ i(\mathrm{m},\mathrm{n}) \neq 0}}^{\mathrm{N}} \int_{\Gamma_{\mathrm{n}}} \frac{\mathbf{v}^{\mathrm{n},i(\mathrm{m},\mathrm{n})}(\mathbf{x}')}{|\mathbf{x}-\mathbf{x}'|}\, \mathrm{d}\Gamma(\mathbf{x}'), \quad \mathbf{x} \in \mathbb{R}^3. \tag{22}$$

Eq. (22) may be recast as

$$\mathbf{A}(\mathbf{x}) \approx \sum_{\mathrm{m}=1}^{\mathrm{M}} \mathrm{I}_{\mathrm{m}}\, \mathbf{g}^{\mathrm{m}}(\mathbf{x}), \quad \mathbf{x} \in \mathbb{R}^3, \tag{23}$$

where

$$\mathbf{g}^{\mathrm{m}}(\mathbf{x}) = \frac{\mu_0}{4\pi} \sum_{\substack{\mathrm{n}=1 \\ i(\mathrm{m},\mathrm{n}) \neq 0}}^{\mathrm{N}} \int_{\Gamma_{\mathrm{n}}} \frac{\mathbf{v}^{\mathrm{n},i(\mathrm{m},\mathrm{n})}(\mathbf{x}')}{|\mathbf{x}-\mathbf{x}'|}\, \mathrm{d}\Gamma(\mathbf{x}'), \quad \mathbf{x} \in \mathbb{R}^3, \quad 1 \leq \mathrm{m} \leq \mathrm{M}. \tag{24}$$

3.5 Magnetic flux density

On using Eqs. (8), (19) and (21), we obtain the following approximation for the magnetic flux density $\mathbf{B}$:

$$\mathbf{B}(\mathbf{x}) \approx \frac{\mu_0}{4\pi} \sum_{\mathrm{n}=1}^{\mathrm{N}} \int_{\Gamma_{\mathrm{n}}} \sum_{\mathrm{j}=1}^{3} \mathrm{I}_{\mathrm{nj}} \frac{-(\mathbf{x}-\mathbf{x}') \times \mathbf{v}^{\mathrm{nj}}(\mathbf{x}')}{|\mathbf{x}-\mathbf{x}'|^3}\, \mathrm{d}\Gamma(\mathbf{x}')$$

$$= \frac{\mu_0}{4\pi} \sum_{\mathrm{m}=1}^{\mathrm{M}} \mathrm{I}_{\mathrm{m}} \sum_{\substack{\mathrm{n}=1 \\ i(\mathrm{m},\mathrm{n}) \neq 0}}^{\mathrm{N}} \int_{\Gamma_{\mathrm{n}}} \frac{-(\mathbf{x}-\mathbf{x}') \times \mathbf{v}^{\mathrm{n},i(\mathrm{m},\mathrm{n})}(\mathbf{x}')}{|\mathbf{x}-\mathbf{x}'|^3}\, \mathrm{d}\Gamma(\mathbf{x}'), \quad \mathbf{x} \in \mathbb{R}^3. \tag{25}$$

Eq. (25) may be expressed as

$$\mathbf{B}(\mathbf{x}) \approx \sum_{\mathrm{m}=1}^{\mathrm{M}} \mathrm{I}_{\mathrm{m}}\, \mathbf{h}^{\mathrm{m}}(\mathbf{x}), \quad \mathbf{x} \in \mathbb{R}^3, \tag{26}$$

where

$$\mathbf{h}^{\mathrm{m}}(\mathbf{x}) = \frac{\mu_0}{4\pi} \sum\nolimits_{\substack{\mathrm{n}=1 \\ i(\mathrm{m},\mathrm{n}) \neq 0}}^{\mathrm{N}} \int_{\Gamma_{\mathrm{n}}} \frac{-(\mathbf{x}-\mathbf{x}') \times \mathbf{v}^{\mathrm{n},i(\mathrm{m},\mathrm{n})}(\mathbf{x}')}{|\mathbf{x}-\mathbf{x}'|^3}\, \mathrm{d}\Gamma(\mathbf{x}'), \quad \mathbf{x} \in \mathbb{R}^3, \quad 1 \le \mathrm{m} \le \mathrm{M}. \tag{27}$$

4 Description of the algorithm

If the z−component of the magnetic flux density **B** is known at L points in the region of interest Ω, as shown in Fig. 3 for cylindrical and hemispherical coil surfaces, then the BEM discretisation of the inverse problem (9) yields the following system of linear algebraic equations

$$\mathbf{H}\,\mathbf{I} = \widetilde{\mathbf{B}}_{\mathrm{z}}. \tag{28}$$

Here $\mathbf{H} \in \mathbb{R}^{\mathrm{L}\times\mathrm{M}}$ is the matrix containing the z−component of the BEM vector $\mathbf{h}^{\mathrm{m}}$ given by Eq. (27) calculated at L points in the region of interest Ω, $\widetilde{\mathbf{B}}_{\mathrm{z}} = \left(\widetilde{\mathrm{B}}_{\mathrm{z}}^{1}, \ldots, \widetilde{\mathrm{B}}_{\mathrm{z}}^{\mathrm{L}}\right)^{\mathrm{T}} \in \mathbb{R}^{\mathrm{L}}$ is a vector containing the z−component of the magnetic flux density at L points in the region of interest Ω and $\mathbf{I} \in \mathbb{R}^{\mathrm{M}}$ is a vector containing the unknown values of the stream function I_{m}, $1 \le \mathrm{m} \le \mathrm{M}$, at the global nodes, i.e.

$$\mathrm{H}_{\mathrm{lm}} = \mathrm{h}_{\mathrm{z}}^{\mathrm{m}}(\mathbf{x}^{\mathrm{l}}) = \frac{\mu_0}{4\pi} \sum\nolimits_{\substack{\mathrm{n}=1 \\ i(\mathrm{m},\mathrm{n}) \neq 0}}^{\mathrm{N}} \int_{\Gamma_{\mathrm{n}}} \frac{1}{|\mathbf{x}^{\mathrm{l}}-\mathbf{x}'|^3} \times \left[(\mathrm{x}^{\mathrm{l}}-\mathrm{x}')\mathrm{v}_{\mathrm{y}}^{\mathrm{n},i(\mathrm{m},\mathrm{n})}(\mathbf{x}') + (\mathrm{y}^{\mathrm{l}}-\mathrm{y}')\mathrm{v}_{\mathrm{x}}^{\mathrm{n},i(\mathrm{m},\mathrm{n})}(\mathbf{x}')\right] \mathrm{d}\Gamma(\mathbf{x}'),$$

$$\widetilde{\mathrm{B}}_{\mathrm{z}}^{\mathrm{l}} = \mathrm{B}_{\mathrm{z}}(\mathbf{x}^{\mathrm{l}}), \quad 1 \le \mathrm{l} \le \mathrm{L}, \quad 1 \le \mathrm{m} \le \mathrm{M}. \tag{29}$$

It is important to mention that the integrals involved in the definition (29) of the components H_{lm} of the BEM matrix **H** are non-singular since $\mathbf{x}^{\mathrm{l}} \notin \Gamma_{\mathrm{coil}}$, $1 \le \mathrm{l} \le \mathrm{L}$, and hence they are evaluated numerically by employing a Gauss quadrature for triangles, see e.g. Brebbia, Telles and Wrobel (1984).

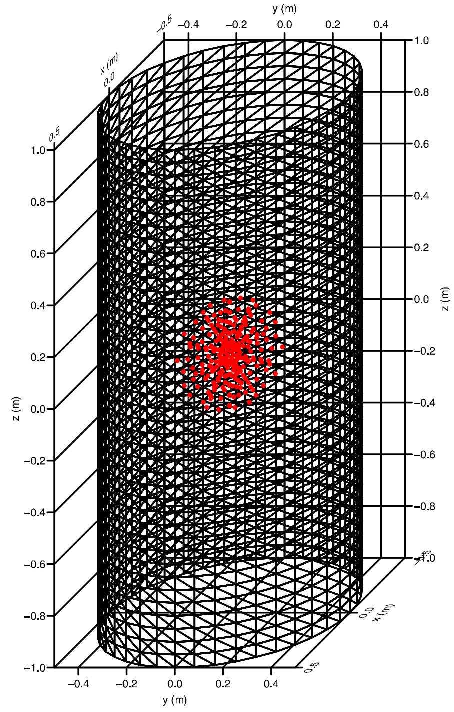

(a)

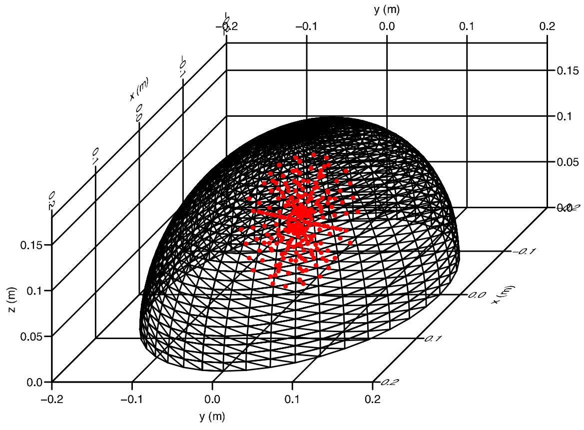

(b)

Figure 3: The BEM mesh used for (a) the cylindrical, and (b) the hemispherical coils, and the location of the internal points (●) in the corresponding spherical region of interest.

4.1 Direct approach

A direct approach to solving the system of linear algebraic equations (28) resulting from the discretization of the present inverse problem can be implemented by, for example, using the least-squares method. In this case, the least-squares solution $\mathbf{I}_{\mathrm{LS}}$ to the inverse problem (9) is sought as, see e.g. Tikhonov and Arsenin (1986),

$$\mathbf{I}_{\mathrm{LS}} \in \mathbb{R}^{\mathrm{M}}: \quad \mathscr{F}_{\mathrm{LS}}(\mathbf{I}_{\mathrm{LS}}) = \min_{\mathbf{I}\in\mathbb{R}^{\mathrm{M}}} \mathscr{F}_{\mathrm{LS}}(\mathbf{I}), \tag{30}$$

where $\mathscr{F}_{\mathrm{LS}}$ is the least-squares functional defined by

$$\begin{aligned} \mathscr{F}_{\mathrm{LS}} :& \mathbb{R}^{\mathrm{M}} \longrightarrow [0,\infty) \\ \mathscr{F}_{\mathrm{LS}}(\mathbf{I}) =& \frac{1}{2}\|\mathbf{H}\,\mathbf{I} - \widetilde{\mathbf{B}}_{\mathrm{z}}\|^2 \\ =& \frac{1}{2}\sum_{\mathrm{l}=1}^{\mathrm{L}} \left(\sum_{\mathrm{m}=1}^{\mathrm{M}} \mathrm{H}_{\mathrm{lm}}\,\mathrm{I}_{\mathrm{m}} - \widetilde{\mathrm{B}}_{\mathrm{z}}^{\mathrm{l}} \right)^2 . \end{aligned} \tag{31}$$

However, the system of linear algebraic equations (28) cannot be solved by a direct approach, such as the least-squares method, since such a method would produce an inaccurate and/or physically meaningless solution due to the large value of the condition number of the system matrix $\mathbf{H}$ which increases dramatically as the BEM mesh is refined. Several regularization procedures have been developed to solve such ill-conditioned systems, see for example Hansen (1998). In the following, we only consider the Tikhonov regularization method and for further details on this method, we refer the reader to Tikhonov and Arsenin (1986).

4.2 Magnetic energy and energy norm

The magnetic energy W defined by

$$\mathrm{W} = \frac{1}{2}\int_{\Gamma_{\mathrm{coil}}} \mathbf{J}^{\mathrm{coil}}(\mathbf{x}) \cdot \mathbf{A}(\mathbf{x})\, \mathrm{d}\Gamma(\mathbf{x}), \tag{32}$$

can be approximated, according to Eqs. (19), (21) and (22), as

$$\begin{aligned} \mathrm{W} \approx& \frac{1}{2}\frac{\mu_0}{4\pi} \sum_{\mathrm{m}'=1}^{\mathrm{N}} \sum_{\mathrm{n}'=1}^{\mathrm{N}} \int_{\Gamma_{\mathrm{m}'}} \int_{\Gamma_{\mathrm{n}'}} \sum_{\mathrm{i}=1}^{3}\sum_{\mathrm{j}=1}^{3} \mathrm{I}_{\mathrm{m}'\mathrm{i}}\,\mathrm{I}_{\mathrm{n}'\mathrm{j}} \\ & \frac{\mathbf{v}^{\mathrm{m}'\mathrm{i}}(\mathbf{x}) \cdot \mathbf{v}^{\mathrm{n}'\mathrm{j}}(\mathbf{x}')}{|\mathbf{x} - \mathbf{x}'|}\, \mathrm{d}\Gamma(\mathbf{x}')\, \mathrm{d}\Gamma(\mathbf{x}) \\ =& \frac{1}{2}\frac{\mu_0}{4\pi} \sum_{\mathrm{m}=1}^{\mathrm{M}} \sum_{\mathrm{n}=1}^{\mathrm{M}} \mathrm{I}_{\mathrm{m}}\,\mathrm{I}_{\mathrm{n}} \sum\nolimits^{\mathrm{N}}{}_{\substack{\mathrm{m}'=1 \\ i(\mathrm{m},\mathrm{m}')\neq 0}} \quad \sum\nolimits^{\mathrm{N}}{}_{\substack{\mathrm{n}'=1 \\ i(\mathrm{n},\mathrm{n}')\neq 0}} \\ & \int_{\Gamma_{\mathrm{m}'}} \int_{\Gamma_{\mathrm{n}'}} \frac{\mathbf{v}^{\mathrm{m}',i(\mathrm{m},\mathrm{m}')}(\mathbf{x}) \cdot \mathbf{v}^{\mathrm{n}',i(\mathrm{n},\mathrm{n}')}(\mathbf{x}')}{|\mathbf{x} - \mathbf{x}'|}\, \mathrm{d}\Gamma(\mathbf{x}')\, \mathrm{d}\Gamma(\mathbf{x}). \end{aligned} \tag{33}$$

Eq. (33) may be recast as

$$\mathrm{W} \approx \frac{1}{2}\sum_{\mathrm{m}=1}^{\mathrm{M}}\sum_{\mathrm{n}=1}^{\mathrm{M}} \mathrm{L}_{\mathrm{mn}}\,\mathrm{I}_{\mathrm{n}}\,\mathrm{I}_{\mathrm{m}}, \tag{34}$$

where the components of the inductance matrix $\mathbf{L} = [\mathrm{L}_{\mathrm{mn}}] \in \mathbb{R}^{\mathrm{M}\times\mathrm{M}}$ are given by

$$\begin{aligned} \mathrm{L}_{\mathrm{mn}} =& \frac{\mu_0}{4\pi} \sum_{\substack{\mathrm{m}'=1 \\ i(\mathrm{m},\mathrm{m}')\neq 0}}^{\mathrm{N}} \sum_{\substack{\mathrm{n}'=1 \\ i(\mathrm{n},\mathrm{n}')\neq 0}}^{\mathrm{N}} \\ & \int_{\Gamma_{\mathrm{m}'}} \int_{\Gamma_{\mathrm{n}'}} \frac{\mathbf{v}^{\mathrm{m}',i(\mathrm{m},\mathrm{m}')}(\mathbf{x}) \cdot \mathbf{v}^{\mathrm{n}',i(\mathrm{n},\mathrm{n}')}(\mathbf{x}')}{|\mathbf{x} - \mathbf{x}'|}\, \mathrm{d}\Gamma(\mathbf{x}')\, \mathrm{d}\Gamma(\mathbf{x}), \\ & 1 \leq \mathrm{m},\mathrm{n} \leq \mathrm{M}. \end{aligned} \tag{35}$$

The evaluation of the double integral involved in the definition (35) of the components L_{mn} of the inductance matrix $\mathbf{L}$ requires special attention since a crude approximation of this integral was used by Lemdiasov and Ludwig (2005). More precisely, in the case of linear triangular elements, i.e. constant interpolation for the current density, Lemdiasov and Ludwig (2005) have approximated the denominator of the integrand by the distance between the centres of mass of the linear triangular elements $\Gamma_{\mathrm{m}'}$ and $\Gamma_{\mathrm{n}'}$, respectively, and hence they reduced the computation of the double integral to calculating the surface area of the linear (flat) triangular elements $\Gamma_{\mathrm{m}'}$ and $\Gamma_{\mathrm{n}'}$. Although this approximation might be suitable for elements located far from one another, it becomes inappropriate for close triangular elements. Consequently, in addition to the ill-posedness of the inverse problem investigated, such an approach induces a significant numerical error and this will affect the accuracy of the solution. Therefore, in this study, the evaluation of the double integral involved in Eq. (35) is performed numerically for the non-singular case, i.e. $\Gamma_{m'} \neq \Gamma_{n'}$, by employing twice the 2D Gauss quadrature for triangles, see e.g. Brebbia, Telles and Wrobel (1984). In the singular case when $\Gamma_{m'} = \Gamma_{n'}$, the outer integral is evaluated numerically using the 2D Gauss quadrature for triangles, whilst for the inner integral the singularity is removed by introducing suitable local polar coordinates and then applying the 1D Gauss-Legendre quadrature, see e.g. Brebbia, Telles and Wrobel (1984).

It should be mentioned that the inductance matrix $\mathbf{L}$ is symmetric, i.e.

$$L_{mn} = L_{mn}, \quad 1 \leq m,n \leq M. \tag{36}$$

Furthermore, it can be shown numerically that the inductance matrix $\mathbf{L}$ is also positive definite, i.e.

$$\begin{cases} \displaystyle\sum_{m=1}^{M}\sum_{n=1}^{M} L_{mn} I_n I_m \geq 0, \\ \qquad \forall\, I_1, I_2, \ldots, I_M \in \mathbb{R} \\ \displaystyle\sum_{m=1}^{M}\sum_{n=1}^{M} L_{mn} I_n I_m = 0 \\ \qquad \Longleftrightarrow\; I_1 = I_2 = \ldots = I_M = 0. \end{cases} \tag{37}$$

The purpose of the regularization techniques is to introduce a smoothing norm and this is strongly related to the magnetic energy W defined by Eq. (32). It should be noted that, since the inductance matrix $\mathbf{L}$ is symmetric and positive definite, see Eqs. (36) and (37), the existence of the square root matrix $\widetilde{\mathbf{L}} \in \mathbb{R}^{M\times M}$ associated to $\mathbf{L}$, i.e. $\widetilde{\mathbf{L}}^2 = \mathbf{L}$, is ensured. Moreover, $\widetilde{\mathbf{L}}$ is also a symmetric matrix, i.e. $\widetilde{\mathbf{L}}^T = \widetilde{\mathbf{L}}$. Consequently, the approximated magnetic energy W given by Eq. (34) is a quadratic and positive definite form which induces the following energy norm:

$$\|\mathbf{I}\|_W^2 = \|\widetilde{\mathbf{L}}\mathbf{I}\|^2 = \sum_{m=1}^{M}\sum_{n=1}^{M} L_{mn} I_n I_m = 2W. \tag{38}$$

4.3 Regularization

The Tikhonov regularized solution $\mathbf{I}_\lambda$ to the inverse problem (9) is sought as, see e.g. Tikhonov and Arsenin (1986),

$$\mathbf{I}_\lambda \in \mathbb{R}^M : \quad \mathscr{F}_\lambda(\mathbf{I}_\lambda) = \min_{\mathbf{I}\in\mathbb{R}^M} \mathscr{F}_\lambda(\mathbf{I}), \tag{39}$$

where $\mathscr{F}_\lambda$ is the Tikhonov functional given by

$$\begin{aligned} \mathscr{F}_\lambda(\cdot) :& \mathbb{R}^M \longrightarrow [0,\infty) \\ \mathscr{F}_\lambda(\mathbf{I}) =& \mathscr{F}_{LS}(\mathbf{I}) + \lambda W \\ =& \frac{1}{2}\|\mathbf{H}\mathbf{I} - \widetilde{\mathbf{B}}_z\|^2 + \frac{1}{2}\lambda\|\mathbf{I}\|_W^2 \\ =& \frac{1}{2}\|\mathbf{H}\mathbf{I} - \widetilde{\mathbf{B}}_z\|^2 + \frac{1}{2}\lambda\|\widetilde{\mathbf{L}}\mathbf{I}\|^2 \\ =& \frac{1}{2}\sum_{l=1}^{L}\left(\sum_{m=1}^{M} H_{lm} I_m - \widetilde{B}_z^l\right)^2 \\ &+ \frac{1}{2}\lambda \sum_{m=1}^{M}\sum_{n=1}^{M} L_{mn} I_n I_m, \end{aligned} \tag{40}$$

with $\lambda > 0$ the regularization parameter to be chosen. Formally, the Tikhonov regularized solution $\mathbf{I}_\lambda$ of the minimisation problem (39) is given by the solution of the regularized normal system of equations

$$\left(\mathbf{H}^T\mathbf{H} + \lambda\widetilde{\mathbf{L}}^T\widetilde{\mathbf{L}}\right)\mathbf{I}_\lambda = \mathbf{H}^T\widetilde{\mathbf{B}}_z, \tag{41}$$

that is

$$\mathbf{I}_\lambda = \left(\mathbf{H}^T\mathbf{H} + \lambda\widetilde{\mathbf{L}}^T\widetilde{\mathbf{L}}\right)^{-1}\mathbf{H}^T\widetilde{\mathbf{B}}_z. \tag{42}$$

Regularization is necessary when solving ill-conditioned systems of linear equations because the simple least-squares solution, i.e. $\lambda = 0$, is completely dominated by contributions from rounding errors. By adding regularization we are able to damp out these contributions and maintain the energy norm $\|\mathbf{I}\|_W = \|\widetilde{\mathbf{L}}\mathbf{I}\|$ to be of reasonable size. If too much regularization, or damping, i.e. λ is large, is imposed on the solution then it will not fit the given data $\widetilde{\mathbf{B}}_z$ properly and the residual norm $\|\mathbf{H}\mathbf{I} - \widetilde{\mathbf{B}}_z\|$ will be too large. If too little regularization is imposed on the solution, i.e. λ is small, then the fit will be good, but the solution will be dominated by the contributions from computational errors, and hence the energy norm

$\|\mathbf{I}\|_W = \|\widetilde{\mathbf{L}}\mathbf{I}\|$ will be too large. To summarize, the Tikhonov regularization method solves a minimisation problem using a smoothness constraint in order to provide a stable solution which fits the data and also has a minimum structure.

5 Numerical results

In this section, we illustrate the results obtained using the numerical method described in Section 4 combined with the divergence-free BEM presented in Section 3 and, in addition, we investigate the convergence and accuracy of the proposed numerical method and also perform a sensitivity analysis with respect to the choice of the regularization parameter.

5.1 Examples

In order to demonstrate the performance of the proposed method, we solve the inverse problem (9) for the following geometries, see also Figs. 3(a) and (b):

Example 1. Consider a cylindrical coil $\Gamma_{\mathrm{coil}} = \{\mathbf{x} = (x,y,z) \in \mathbb{R}^3 \,|\, x^2 + y^2 = R^2, -h \le z \le h\}$, where $R = 0.5\,\mathrm{m}$ and $h = 1.0\,\mathrm{m}$, while the region of interest is a sphere centered at the origin of the coordinate system, i.e. $\Omega = \{\mathbf{x} = (x,y,z) \in \mathbb{R}^3 \,|\, x^2 + y^2 + z^2 \le r^2\}$, where $r = 0.2\,\mathrm{m}$.

Example 2. Consider a hemispherical coil $\Gamma_{\mathrm{coil}} = \{\mathbf{x} = (x,y,z) \in \mathbb{R}^3 \,|\, x^2 + y^2 + z^2 = R^2, z \ge 0\}$, where $R = 0.175\,\mathrm{m}$. Here the region of interest is a sphere centered at $\mathbf{x}^c = (x^c, y^c, z^c) = (0, 0, 0.081)$, i.e. $\Omega = \{\mathbf{x} = (x,y,z) \in \mathbb{R}^3 \,|\, (x - x^c)^2 + (y - y^c)^2 + (z - z^c)^2 \le r^2\}$, where $r = 0.065\,\mathrm{m}$.

Since the geometries of the two types of coil considered in this paper are symmetrical with respect to the z−axis, it is sufficient to investigate only the design of x− and z−gradients, i.e.

$$\widetilde{B}_z(\mathbf{x}) = G_x\, x, \quad \widetilde{B}_z(\mathbf{x}) = G_z\, z, \quad \mathbf{x} \in \Omega, \tag{43}$$

where $G_x \in \mathbb{R}$ and $G_z \in \mathbb{R}$ are given. Although not presented herein, it is reported that the numerical results obtained for the cylindrical and hemispherical y−gradient coils are similar to those retrieved for the corresponding x−gradient coils, but rotated by an angle $\theta = \pi/2$ about the z−axis. For the present computations, we have considered $G_x = G_z = 1.0\,\mathrm{T\,m^{-1}}$.

The numerical results presented in this section have been obtained using three different BEM meshes for the coil surface Γ_{coil}, namely $N \in \{1152, 2048, 3200\}$ and $N \in \{1128, 1888, 2840\}$ triangular boundary elements for the cylindrical and hemispherical coils, respectively. It should be noted that the aforementioned BEM meshes correspond to $M \in \{600, 1056, 1640\}$ and $M \in \{577, 961, 1441\}$ global nodes on the cylindrical and hemispherical coil surfaces, respectively, used for the approximation of the unknown stream function $\mathbf{I} = (I_1, I_2, \ldots, I_M)^T$. Moreover, for both coil geometries analysed in this study, the z−component of the magnetic flux density is known at $L = 351$ internal points in the corresponding spherical region of interest.

5.2 Reduction of the regularized system of normal equations

It is important to mention that the dimension of the regularized system of normal equations (41) can be decreased for the coil surfaces analysed in this paper due to the fact that these are not closed surfaces and there is no current flux flowing into or out of the coil surface. More precisely, the cylindrical and hemispherical coil surfaces considered are bounded by the following 3D curves:

Example 1. Cylindrical coil ($R = 0.5\,\mathrm{m}$ and $h = 1.0\,\mathrm{m}$):

$$\begin{aligned} &\partial\Gamma_{\mathrm{coil}} = \gamma^{(1)}_{\mathrm{coil}} \cup \gamma^{(2)}_{\mathrm{coil}} : \\ &\gamma^{(1)}_{\mathrm{coil}} = \{\mathbf{x} = (x,y,z) \in \mathbb{R}^3 \,|\, x^2 + y^2 = R^2, z = -h\} \\ &\gamma^{(2)}_{\mathrm{coil}} = \{\mathbf{x} = (x,y,z) \in \mathbb{R}^3 \,|\, x^2 + y^2 = R^2, z = h\}. \end{aligned} \tag{44}$$

Example 2. Hemispherical coil ($R = 0.175\,\mathrm{m}$):

$$\begin{aligned} &\partial\Gamma_{\mathrm{coil}} = \gamma^{(1)}_{\mathrm{coil}} \\ &\gamma^{(1)}_{\mathrm{coil}} = \{\mathbf{x} = (x,y,z) \in \mathbb{R}^3 \,|\, x^2 + y^2 = R^2, z = 0\}. \end{aligned} \tag{45}$$

In order to derive the discrete condition for the stream function associated with the global nodes that belong to a curve bounding the coil surface, i.e. $\gamma_{\mathrm{coil}}^{(\mathrm{j})} \subset \partial\Gamma_{\mathrm{coil}}$, we consider a triangular boundary element $\Gamma_{\mathrm{n}} = \triangle \mathbf{x}^{\mathrm{n1}}\mathbf{x}^{\mathrm{n2}}\mathbf{x}^{\mathrm{n3}} \subset \Gamma_{\mathrm{coil}}$ and, without any loss of the generality, assume that $\Gamma_{\mathrm{n}} \cap \gamma_{\mathrm{coil}}^{(\mathrm{j})} = \left\{\mathbf{x}^{\mathrm{n2}}, \mathbf{x}^{\mathrm{n3}}\right\}$, see Fig. 1. On considering ν^{n1} the outward unit vector normal to the edge Γ_{n1} opposite to the local node $\mathbf{x}^{\mathrm{n1}}$ and lying in the plane tangent to the triangular boundary element Γ_{n}, see also Fig. 1, we obtain:

$$\begin{aligned}
0 = {} & \mathbf{J}^{\mathrm{coil}}(\mathbf{x})\big|_{\Gamma_{\mathrm{n1}}} \cdot \nu^{\mathrm{n1}}(\mathbf{x}) \\
\approx {} & \left[\mathrm{I}_{\mathrm{n1}}\, \mathbf{v}^{\mathrm{n1}}(\mathbf{x}) + \mathrm{I}_{\mathrm{n2}}\, \mathbf{v}^{\mathrm{n2}}(\mathbf{x}) + \mathrm{I}_{\mathrm{n3}}\, \mathbf{v}^{\mathrm{n3}}(\mathbf{x})\right] \cdot \nu^{\mathrm{n1}}(\mathbf{x}) \\
= {} & [\mathrm{I}_{\mathrm{n1}}\, \mathbf{v}^{\mathrm{n1}}(\mathbf{x}) + \mathrm{I}_{\mathrm{n2}}\, \underbrace{\left(\mathbf{v}^{\mathrm{n1}}(\mathbf{x}) + \mathbf{v}^{\mathrm{n2}}(\mathbf{x}) + \mathbf{v}^{\mathrm{n3}}(\mathbf{x})\right)}_{=0 \text{ according to Eq. (15)}} \\
& - \mathrm{I}_{\mathrm{n2}}\, \left(\mathbf{v}^{\mathrm{n1}}(\mathbf{x}) + \mathbf{v}^{\mathrm{n3}}(\mathbf{x})\right) + \mathrm{I}_{\mathrm{n3}}\, \mathbf{v}^{\mathrm{n3}}(\mathbf{x})] \cdot \nu^{\mathrm{n1}}(\mathbf{x}) \\
= {} & (\mathrm{I}_{\mathrm{n1}} - \mathrm{I}_{\mathrm{n2}})\, \underbrace{\left[\mathbf{v}^{\mathrm{n1}}(\mathbf{x}) \cdot \nu^{\mathrm{n1}}(\mathbf{x})\right]}_{=0 \text{ by definition}} \\
& + (\mathrm{I}_{\mathrm{n3}} - \mathrm{I}_{\mathrm{n2}})\, \left[\mathbf{v}^{\mathrm{n3}}(\mathbf{x}) \cdot \nu^{\mathrm{n1}}(\mathbf{x})\right] \\
= {} & (\mathrm{I}_{\mathrm{n3}} - \mathrm{I}_{\mathrm{n2}})\, \left[\mathbf{v}^{\mathrm{n3}}(\mathbf{x}) \cdot \nu^{\mathrm{n1}}(\mathbf{x})\right] .
\end{aligned} \tag{46}$$

Since $\mathbf{v}^{\mathrm{n3}}(\mathbf{x}) \cdot \nu^{\mathrm{n1}}(\mathbf{x}) \neq 0$, from Eq. (46) it follows that

$$\mathrm{I}_{\mathrm{n2}} = \mathrm{I}_{\mathrm{n3}}. \tag{47}$$

By extending this rationale to all the triangular boundary elements that share two nodes with the curve $\gamma_{\mathrm{coil}}^{(\mathrm{j})} \subset \partial\Gamma_{\mathrm{coil}}$, we obtain the discrete condition for the stream function associated with the global nodes that belong to a curve bounding the coil surface, namely

$$\mathrm{I}_{\mathrm{m}_1} = \mathrm{I}_{\mathrm{m}_2} = \ldots = \mathrm{I}_{\mathrm{m}_\mathrm{j}}, \quad \mathbf{x}^{\mathrm{m}_1}, \mathbf{x}^{\mathrm{m}_2}, \ldots, \mathbf{x}^{\mathrm{m}_\mathrm{j}} \in \gamma_{\mathrm{coil}}^{(\mathrm{j})}. \tag{48}$$

Consequently, if the coil surface Γ_{coil} under consideration is bounded by the 3D curves $\gamma_{\mathrm{coil}}^{(\mathrm{j})}$, $1 \leq \mathrm{j} \leq \mathrm{J}$, such that $\mathrm{m_j}$ global nodes are located on each curve $\gamma_{\mathrm{coil}}^{(\mathrm{j})}$, $1 \leq \mathrm{j} \leq \mathrm{J}$, then the original dimension M of the regularized system of normal equations (41) is reduced to $\widetilde{\mathrm{M}} = \mathrm{M} - \sum_{\mathrm{j}=1}^{\mathrm{J}} \left(\mathrm{m_j} - 1\right)$. It is worth mentioning that the dimensions of the matrices $\mathbf{H}$ and $\mathbf{L}$ involved in the original regularized system of normal equations (41), as well as the unknown stream function vector $\mathbf{I}$, should be reduced accordingly.

5.3 Selection of the optimal regularization parameter

The choice of the regularization parameter λ in the minimisation process of the Tikhonov functional (40) is crucial for obtaining a stable, accurate and physically correct numerical solution $\mathbf{I}_\lambda$ and this issue was not addressed in a rigorous manner by Lemdiasov and Ludwig (2005). As mentioned in Section 4.3, the optimal value λ_{opt} of the regularization parameter λ should be chosen such that a trade-off between the two quantities $\|\mathbf{HI} - \widetilde{\mathbf{B}}_{\mathrm{z}}\|$ and $\|\mathbf{I}\|_{\mathrm{W}} = \|\widetilde{\mathbf{L}}\mathbf{I}\|$ involved in the minimisation of the functional (40) is attained.

To achieve this, we introduce a term that characterises the difference between the computed and desired z−components of the magnetic flux density in the region of interest, i.e. the relative percentage error defined by

$$\mathrm{err}\left(\mathrm{B_z}(\mathbf{x}); \lambda\right) = \frac{|\mathrm{B}_{\mathrm{z}}^{\lambda}(\mathbf{x}) - \widetilde{\mathrm{B}}_{\mathrm{z}}(\mathbf{x})|}{|\widetilde{\mathrm{B}}_{\mathrm{z}}(\mathbf{x})|} \times 100, \quad \mathbf{x} \in \Omega, \tag{49}$$

where $\mathrm{B}_{\mathrm{z}}^{\lambda}(\mathbf{x})$ is the numerical z−component of the magnetic flux density calculated at the point $\mathbf{x}$ in the region of interest Ω, for a given regularization parameter λ, by employing the BEM-based algorithm described in Section 4. Furthermore, we define a global measure for the percentage relative error $\mathrm{err}\left(\mathrm{B_z}(\mathbf{x}); \lambda\right)$ given by Eq. (49) in the region of interest Ω, namely the maximum relative percentage error

$$\mathrm{Err}\left(\mathrm{B_z}; \lambda\right) = \max_{\mathbf{x} \in \Omega} \mathrm{err}\left(\mathrm{B_z}(\mathbf{x}); \lambda\right). \tag{50}$$

On assuming that a deviation $\varepsilon > 0$ from the desired z−component of the magnetic flux density $\widetilde{\mathrm{B}}_{\mathrm{z}}$ is admissible in the region of interest Ω, such that

$$\widetilde{\mathrm{B}}_{\mathrm{z}}^{\varepsilon}(\mathbf{x}) := \widetilde{\mathrm{B}}_{\mathrm{z}}(\mathbf{x})\,(1 \pm \varepsilon), \quad \mathbf{x} \in \Omega, \tag{51}$$

then the choice of the optimal regularization parameter $\lambda_{\rm opt}$ is made by employing the maximum relative percentage error given by Eq. (50) and the admissible level of variation in $\mathrm{B_z}|_{\Omega}$ defined by relation (51), namely

$$\lambda_{\rm opt} = \max\left\{\lambda > 0 \middle| \mathrm{Err}\left(\mathrm{B_z};\lambda\right) \leq \varepsilon\right\}. \qquad (52)$$

Figs. 4(a) and (b) illustrate the maximum relative percentage error $\mathrm{Err}\left(\mathrm{B_z};\lambda\right)$, as a function of the regularization parameter λ, obtained using quadratic triangular boundary elements for the cylindrical x$-$ and z$-$gradient coils, respectively. It can be seen from these figures that the error $\mathrm{Err}\left(\mathrm{B_z};\lambda\right)$ decreases as the regularization parameter λ tends to zero. The optimal value of the regularization parameter, chosen according to Eq. (52) and corresponding to a deviation of $\varepsilon = 5\%$ from the linearity of the x$-$ and z$-$gradients, is given by $\lambda_{\rm opt} \approx 4.0 \times 10^{-9}$ and $\lambda_{\rm opt} \approx 3.0 \times 10^{-8}$ in the case of the cylindrical x$-$ and z$-$gradient coils, respectively. Although not presented herein, it is reported that a similar evolution of the error $\mathrm{Err}\left(\mathrm{B_z};\lambda\right)$ with respect to the regularization parameter λ has been obtained for the cylindrical x$-$ and z$-$gradient coils when using linear triangular boundary elements, as well as for the hemispherical x$-$ and z$-$gradient coils and both boundary elements investigated in this paper.

5.4 Comparison of the boundary elements

The numerical solution $\mathbf{I}_{\lambda}$ of the regularized system of normal equations (41), with $\lambda = \lambda_{\rm opt}$ given by Eq. (52), provides only a discrete distribution of the stream function at the global nodes of the BEM mesh employed. However, these discrete values should be extended to a continuous distribution of the numerical stream function over the entire coil surface $\Gamma_{\rm coil}$ and this is achieved by employing the contours of the stream function using its discrete distribution and the Matlab (The Mathworks, Inc., Natick, MD, USA) contouring function. Hence, in the sequel, the numerically retrieved solutions of the inverse problem given by Eq. (9) are presented in terms of the contours of the stream function as described above.

Figs. 5(a) and (b) present the 2D contours of the stream function in the $\theta - \mathrm{z}$ plane corresponding to the cylindrical x$-$ and z$-$gradient coils, respectively, obtained using the optimal regularization parameter $\lambda_{\rm opt}$ given by Eq. (52), $\mathrm{L} = 351$ internal points in the region of interest and $\mathrm{N} = 3200$ linear and quadratic triangular boundary elements. Here $\mathrm{z} \in [-1,1]$ and $\theta \in (-\pi,\pi]$ are the height and azimuthal cylindrical coordinates, respectively. Although the contours of the stream function retrieved with linear and quadratic triangular boundary elements cannot be graphically distinguished in the case of the cylindrical x$-$gradient coil, see Fig. 5(a), it is reported that their corresponding values differ. The stream function intensities at various global nodes with cylindrical coordinates $z = 0.5$ and $\theta \in [0,\pi]$, obtained for the cylindrical x$-$gradient coil using linear and quadratic triangular boundary elements, are tabulated in Tab. 1. However, in the case of the cylindrical z$-$gradient coil, the differences between the contours of the stream function obtained with linear and quadratic triangular boundary elements can be noticed graphically from Fig. 5(b), whilst Tab. 2 presents the numerical values for the stream function intensity at various global nodes with cylindrical coordinates $z \in [0,\pi]$ and $\theta = 0$, retrieved by employing the aforementioned triangular boundary elements.

The numerical results for the stream function in the $\theta - \cos\phi$ plane corresponding to the hemispherical x$-$ and z$-$gradient coils, obtained with $\lambda = \lambda_{\rm opt}$ chosen according to Eq. (52), $\mathrm{L} = 351$ internal points in the region of interest and $\mathrm{N} = 2840$ linear and quadratic triangular boundary elements and illustrated in Figs. 6(a) and (b), respectively, emphasize an improvement in the quantitative results when using the latter. Here $\theta \in [0,2\pi)$ and $\phi \in [0,\pi/2]$ are the azimuthal and colatitude spherical coordinates, respectively. It should be noted that, in the case of the hemispherical coil, the so-called Lambert cylindrical equal-area projection, i.e. the $\theta - \cos\phi$ plane, has been used to represent the 2D contours of the stream function. A similar conclusion can be drawn from Tabs. 3 and 4 which present the numerical values for the stream function intensity at various

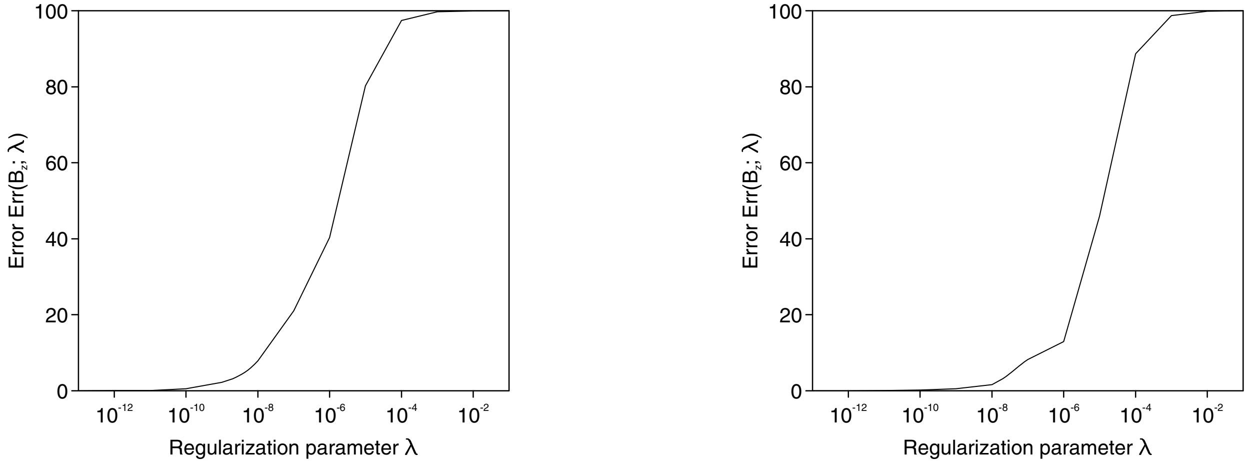

(a) (b)

Figure 4: The maximum relative percentage error $\mathrm{Err}\left(\mathrm{B_z};\lambda\right)$, as a function of the regularization parameter λ, obtained using quadratic triangular boundary elements, for the cylindrical (a) x−, and (b) z−gradient coils.

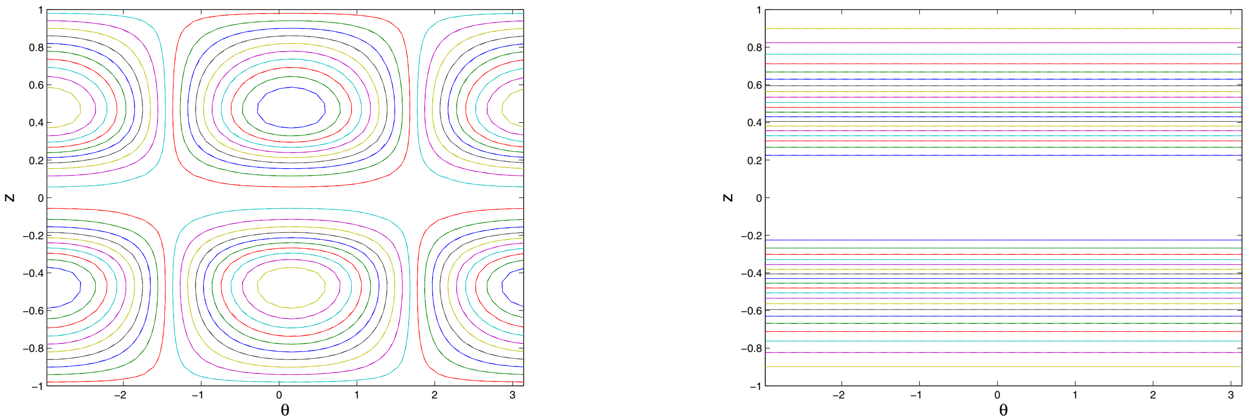

(a) (b)

Figure 5: The contours of the stream function corresponding to the cylindrical (a) x−, and (b) z−gradient coils given by Example 1, obtained using the optimal regularization parameter λ_{opt} chosen according to Eq. (52), $\mathrm{L} = 351$ internal points in the region of interest and $\mathrm{N} = 3200$ linear (—) and quadratic (− −) triangular boundary elements.

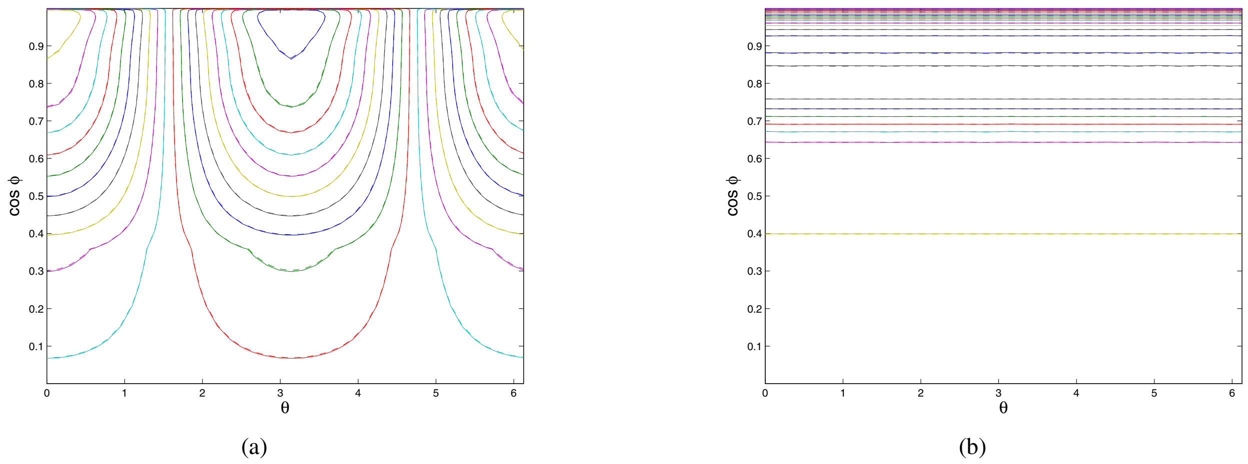

(a) (b)

Figure 6: The contours of the stream function corresponding to the hemispherical (a) x−, and (b) z−gradient coils given by Example 2, obtained using the optimal regularization parameter λ_{opt} chosen according to Eq. (52), L = 351 internal points in the region of interest and N = 2840 linear (—) and quadratic (− −) triangular boundary elements.

global nodes with spherical coordinates $\theta \in [0,\pi]$ and $\phi = 0.1047197$ in the case of the hemispherical x−gradient coil, and $\theta = 0$ and $\phi \in [0,\pi/4]$ in the case of the hemispherical z−gradient coil, respectively, retrieved using linear and quadratic triangular boundary elements.

From Figs. 5 and 6, and Tabs. 1-4 we can conclude that, for the examples investigated in this study, the numerical results retrieved using linear boundary elements are different from those obtained by employing quadratic boundary elements. It should be stressed that, for a given number of triangular boundary elements, the number of collocation points corresponding to the linear approximations (i.e. quadratic boundary elements) for the surface current density, see Eq. (19), remains unchanged and, therefore, the dimension of the resulting BEM system of linear algebraic equations will not be affected. Consequently, the increase of the degree of approximation in Eq. (19) does not affect significantly the computational cost.

5.5 *Influence of the regularization parameter*

It is interesting to investigate how the Tikhonov regularization functional presented in Section 4.3 improves the accuracy of the numerical results, as well as the importance of an appropriate criterion for choosing the optimal regularization parameter. To do so, we consider the cylindrical x−gradient and the hemispherical z−gradient coils only.

Figs. 7(a)-(c) show the 2D contours of the stream function in the $z-\theta$ plane, obtained using N = 3200 quadratic triangular boundary elements, i.e. $N_e = 6$ local nodes and M = 1640 global nodes, L = 351 internal points in the region of interest and various values of the regularization parameter, namely $\lambda = 1.0 \times 10^{-2} > \lambda_{\text{opt}}$, $\lambda = 4.0 \times 10^{-9} \approx \lambda_{\text{opt}}$, and $\lambda = 1.0 \times 10^{-11} < \lambda_{\text{opt}}$, respectively, for the cylindrical x−gradient coil given by Example 1. From Figs. 7(a) and (b), it can be seen that the numerical solution $\mathbf{I}_\lambda$ corresponding to a large value of the regularization parameter, i.e. $\lambda > \lambda_{\text{opt}}$, yields contours of the stream function with a low energy norm, but which do not fit the desired z−component of the magnetic flux density in the region of interest. In contrast, the numerical solution $\mathbf{I}_\lambda$ associated with a very small value of the regularization parameter, i.e. $\lambda < \lambda_{\text{opt}}$, yields contours of the stream function with an oscillatory behaviour, i.e. the corresponding energy norm is high, although the fit with the desired z−component of the magnetic flux density in the region of interest is very good, see Figs.

Table 1: Stream function intensities at various global nodes with cylindrical coordinates $\theta \in [0,\pi]$ and $z = 0.5$, obtained using linear and quadratic triangular boundary elements, for the cylindrical x−gradient coil.

θ	z	I_m (Linear)	I_m (Quadratic)
0.0	0.5	353465.02	354703.80
0.3141592	0.5	336181.12	337359.76
0.6283185	0.5	285987.11	286990.23
0.9424778	0.5	207800.77	208530.18
1.2566371	0.5	109271.83	109656.14
1.5707963	0.5	47.580664	49.164221
1.8849556	0.5	−109181.57	−109562.86
2.1991149	0.5	−207723.78	−208450.63
2.5132741	0.5	−285931.32	−286932.58
2.8274334	0.5	−336151.72	−337329.38
3.1415927	0.5	−353465.02	−354703.80

Table 2: Stream function intensities at various global nodes with cylindrical coordinates $\theta = 0$ and $z \in [0,1]$, obtained using linear and quadratic triangular boundary elements, for the cylindrical z−gradient coil.

θ	z	I_m (Linear)	I_m (Quadratic)
0.0	0.0	−378954.18	−380012.32
0.0	0.1	−382388.77	−383343.89
0.0	0.2	−373138.04	−373949.35
0.0	0.3	−328871.62	−329649.95
0.0	0.4	−259007.31	−259774.38
0.0	0.5	−186144.83	−186830.58
0.0	0.6	−124338.51	−124880.77
0.0	0.7	−77080.789	−77460.616
0.0	0.8	−42616.230	−42845.350
0.0	0.9	−17862.255	−17964.500
0.0	1.0	0.55×10^{-6}	-0.11×10^{-6}

Table 3: Stream function intensities at various global nodes with spherical coordinates $\theta \in [0,\pi]$ and $\phi = 0.1047197$, obtained using linear and quadratic triangular boundary elements, for the hemispherical x−gradient coil.

θ	ϕ	I_m (Linear)	I_m (Quadratic)
0.0	0.1047197	5353.7563	5332.4342
0.3141592	0.1047197	5093.1493	5073.0378
0.6283185	0.1047197	4334.0922	4317.1723
0.9424778	0.1047197	3150.6887	3138.6054
1.2566371	0.1047197	1658.9522	1652.8974
1.5707963	0.1047197	4.7721438	5.3324730
1.8849556	0.1047197	−1649.8512	−1642.7282
2.1991149	0.1047197	−3142.9672	−3129.9773
2.5132741	0.1047197	−4328.4675	−4310.8874
2.8274334	0.1047197	−5090.2000	−5069.7421
3.1415927	0.1047197	−5353.7563	−5332.4342

Table 4: Stream function intensities at various global nodes with spherical coordinates $\theta = 0$ and $\phi \in [0,\pi/4]$, obtained using linear and quadratic triangular boundary elements, for the hemispherical z−gradient coil.

θ	ϕ	I_m (Linear)	I_m (Quadratic)
0.0	0.0	18978.698	19012.141
0.0	0.0261799	19006.000	19037.969
0.0	0.0785398	18845.953	18866.941
0.0	0.1047197	18383.360	18395.162
0.0	0.3141592	15873.713	15911.133
0.0	0.5235987	8917.7579	8905.8097
0.0	0.7330382	3581.8981	3634.0051
0.0	1.0471976	−1654.3486	−1695.5283
0.0	1.1519173	−12815.955	−12898.754
0.0	1.3613568	−25533.014	−25631.409
0.0	1.5184364	−10755.624	−10792.625

7(b) and (c).

A similar conclusion can be drawn from Figs. 8(a)-(c) which illustrate the 2D contours of the stream function in the $\theta - \cos\phi$ plane, obtained using N = 2840 quadratic triangular boundary elements, i.e. $N_e = 6$ local nodes and M = 1441 global nodes, L = 351 internal points in the region of interest and various values of the regularization parameter, namely $\lambda = 1.0 \times 10^{-2} > \lambda_{opt}$, $\lambda = 7.0 \times 10^{-9} \approx \lambda_{opt}$, and $\lambda = 1.0 \times 10^{-11} < \lambda_{opt}$, respectively, for the hemispherical z−gradient coil given by Example 1.

5.6 *Convergence of the method*

The convergence of the proposed numerical method with respect to refining the BEM mesh size is illustrated in Figs. 9(a) and (b) which represent the contours of the stream function corresponding to the cylindrical x− and z−gradient coils, respectively, obtained using the optimal regularization parameter λ_{opt} chosen according to Eq. (52), L = 351 internal points in the region

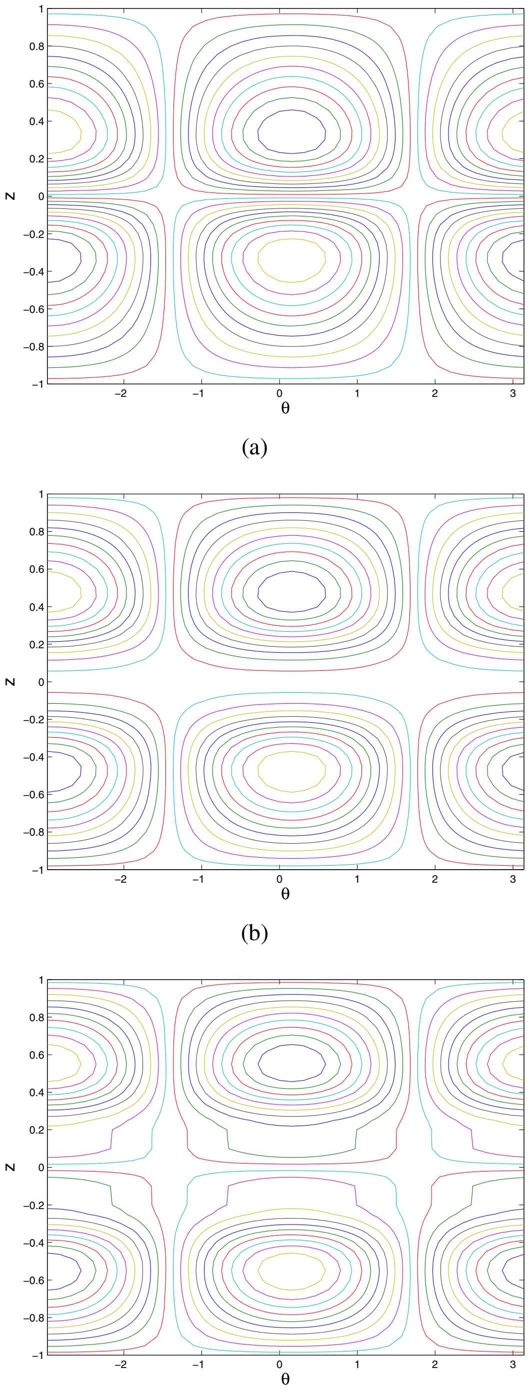

(a)

(b)

(c)

Figure 7: The contours of the stream function obtained using N = 3200 quadratic triangular boundary elements, i.e. $N_e = 6$ local nodes and M = 1640 global nodes, L = 351 internal points in the region of interest and various values of the regularization parameter, namely (a) $\lambda = 1.0 \times 10^{-2} > \lambda_{\text{opt}}$, (b) $\lambda = 4.0 \times 10^{-9} \approx \lambda_{\text{opt}}$, and (c) $\lambda = 1.0 \times 10^{-11} < \lambda_{\text{opt}}$, for the cylindrical x−gradient coil given by Example 1.

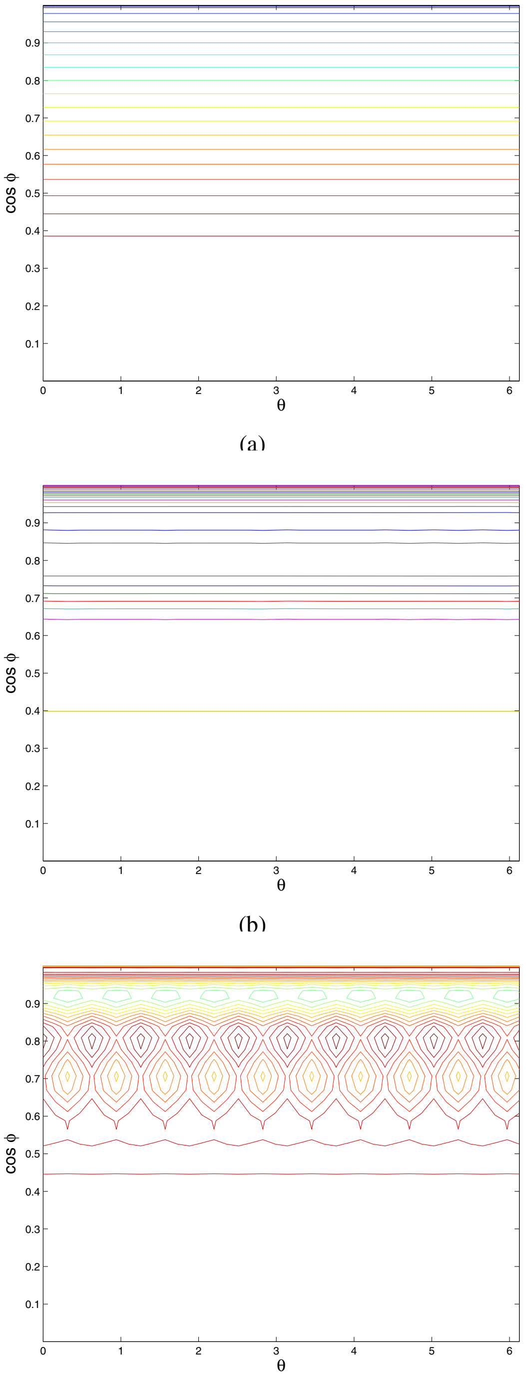

(a)

(b)

(c)

Figure 8: The contours of the stream function obtained using N = 2840 quadratic triangular boundary elements, i.e. $N_e = 6$ local nodes and M = 1441 global nodes, L = 351 internal points in the region of interest and various values of the regularization parameter, namely (a) $\lambda = 1.0 \times 10^{-2} > \lambda_{\text{opt}}$, (b) $\lambda = 7.0 \times 10^{-9} \approx \lambda_{\text{opt}}$, and (c) $\lambda = 1.0 \times 10^{-11} < \lambda_{\text{opt}}$, for the hemispherical z−gradient coil given by Example 2.

of interest and various numbers of quadratic triangular boundary elements ($\mathrm{N_e} = 6$), namely $\mathrm{N} \in \{1152, 2084, 3200\}$. Although an analytical solution for the contours of the stream function is not available, we can conclude from these figures that the Tikhonov regularization method described in Section 4, in conjunction with the divergence-free BEM presented in Section 3, is convergent with respect to increasing the number of boundary elements used to discretise the coil surface Γ_{coil}. Furthermore, the finer the BEM mesh size is then the smoother contours of the stream function corresponding to the cylindrical x$-$ and z$-$gradient coils. Similar results have been obtained for the hemispherical x$-$ and z$-$gradient coils with $\lambda = \lambda_{\mathrm{opt}}$ given by Eq. (52), $\mathrm{L} = 351$ internal points in the region of interest and various numbers of quadratic triangular boundary elements, i.e. $\mathrm{N} \in \{1128, 1888, 2840\}$, and these are shown in Figs. 10(a) and (b), respectively.

There are a number of inter-related parameters characterising the performance of a gradient coil. One of the most important of these is the gradient coil *efficiency*, η, which is the gradient strength produced by the current, I, i.e.

$$\eta = \frac{\mathrm{G}}{I}, \tag{53}$$

where $\mathrm{G} = \mathrm{G_x}$ and $\mathrm{G} = \mathrm{G_z}$ in the case of x$-$ and z$-$gradient coils, respectively. Ideally, the gradient coil efficiency, η, should be as large as possible, but its magnitude is however strongly related to another parameter that plays an important role in gradient coil performance, namely the *inductance*, L, of the gradient coil.

The inductance value is crucial in the design of gradient coils since it limits the rate of change of current in the coil and thus dictates the maximum possible rate of change of gradient per unit time, $\mathrm{dG}/\mathrm{d}t$, that can be achieved. Using a gradient amplifier capable of generating a maximum voltage, V, gives

$$\frac{\mathrm{dG}}{\mathrm{d}t} = \frac{\eta V}{L}, \tag{54}$$

so that the rise-time, τ, required to ramp-up a gradient to amplitude, G, is obtained by integrating Eq. (54) as

$$\tau = \frac{\mathrm{G}L}{\eta V}. \tag{55}$$

This indicates that achieving short rise-times requires gradient coils with low inductance and amplifiers capable of producing high voltages. Using short rise-times means that less time is wasted in ramping up gradients in MR sequences and this often implies faster image acquisition and improved signal to noise ratio. The inductance can be made small by using a small number of turns, n, in the gradient coil since for any coil L is proportional to n^2, but since in addition η is proportional to n, this entails a reduction of the gradient coil efficiency and, therefore, a reduced maximum achievable gradient.

A useful parameter in characterising the performance of gradient coils is the ratio η^2/L, which is independent of the number of turns and indicates the efficiency that can be achieved for a given inductance. It should be mentioned that the inductance, L, is related to the magnetic energy, W, and the current, I, through the following relation:

$$\mathrm{W} = \frac{1}{2} L I^2 \tag{56}$$

and hence, on using Eqs. (53) and (56), we obtain:

$$\frac{\eta^2}{L} = \frac{\mathrm{G}}{2\mathrm{W}}. \tag{57}$$

Figs. 11(a) and (b) present the parameter η^2/L given by Eq. (57) corresponding to the cylindrical x$-$gradient coil and hemispherical z$-$gradient coil, respectively, obtained using the optimal regularization parameter λ_{opt} chosen according to Eq. (52) and $\mathrm{L} = 351$ internal points in the region of interest, as a function of the number of linear ($\mathrm{N_e} = 3$) and quadratic ($\mathrm{N_e} = 6$) triangular boundary elements. It should be mentioned that in Eq. (57) the magnetic energy has been evaluated numerically by employing relations (34) and (35), whilst $\mathrm{G} = \mathrm{G_x} = 1.0\,\mathrm{T\,m^{-1}}$ and $\mathrm{G} = \mathrm{G_z} = 1.0\,\mathrm{T\,m^{-1}}$ in the case of x$-$ and z$-$gradient coils, respectively. From these figures it can be seen that, for both linear and quadratic triangular

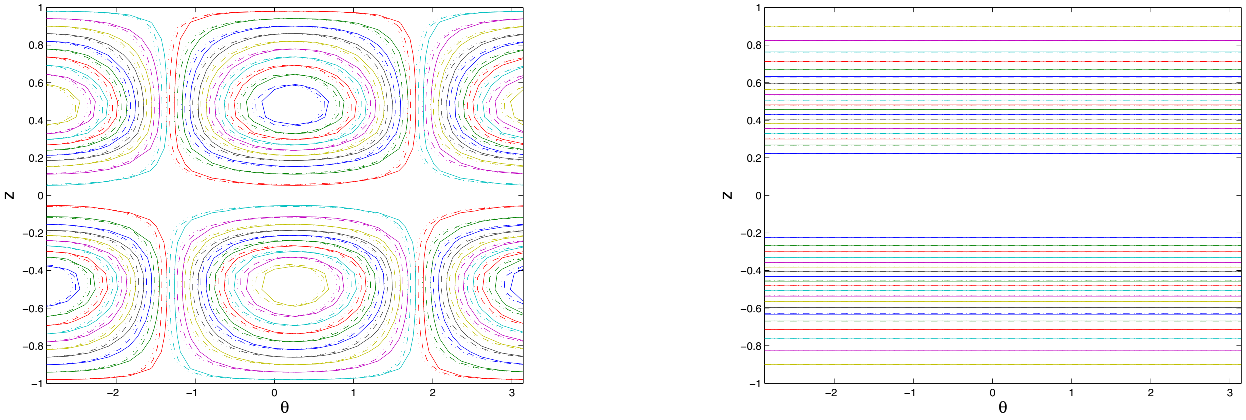

(a) (b)

Figure 9: The contours of the stream function corresponding to the cylindrical (a) x−, and (b) z−gradient coils given by Example 1, obtained using the optimal regularization parameter λ_{opt} chosen according to Eq. (52), $L = 351$ internal points in the region of interest and various numbers of quadratic triangular boundary elements, i.e. $N_e = 6$, namely $N = 1152$ (—), $N = 2084$ (− −) and $N = 3200$ (···).

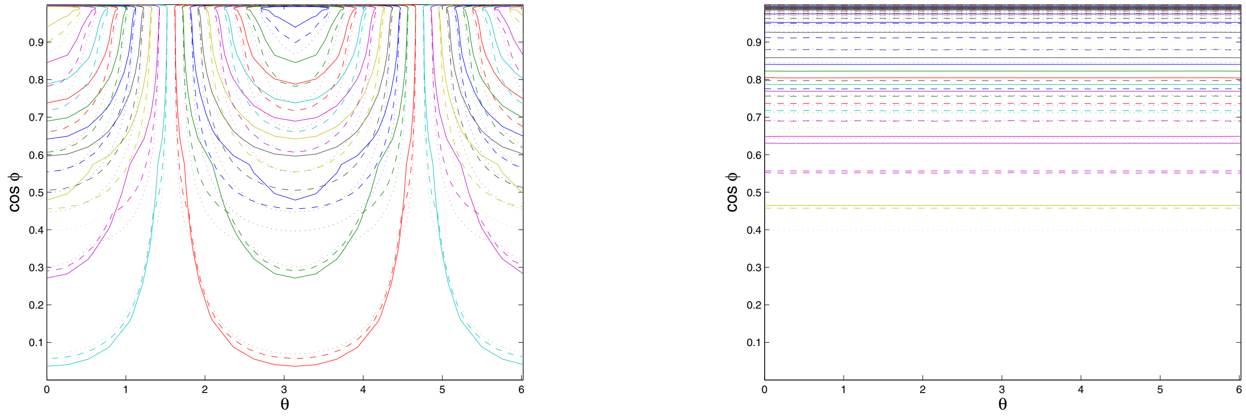

(a) (b)

Figure 10: The contours of the stream function corresponding to the hemispherical (a) x−, and (b) z−gradient coils given by Example 2, obtained using the optimal regularization parameter λ_{opt} chosen according to Eq. (52), $L = 351$ internal points in the region of interest and various numbers of quadratic triangular boundary elements, i.e. $N_e = 6$, namely $N = 1128$ (—), $N = 1888$ (− −) and $N = 2840$ (···).

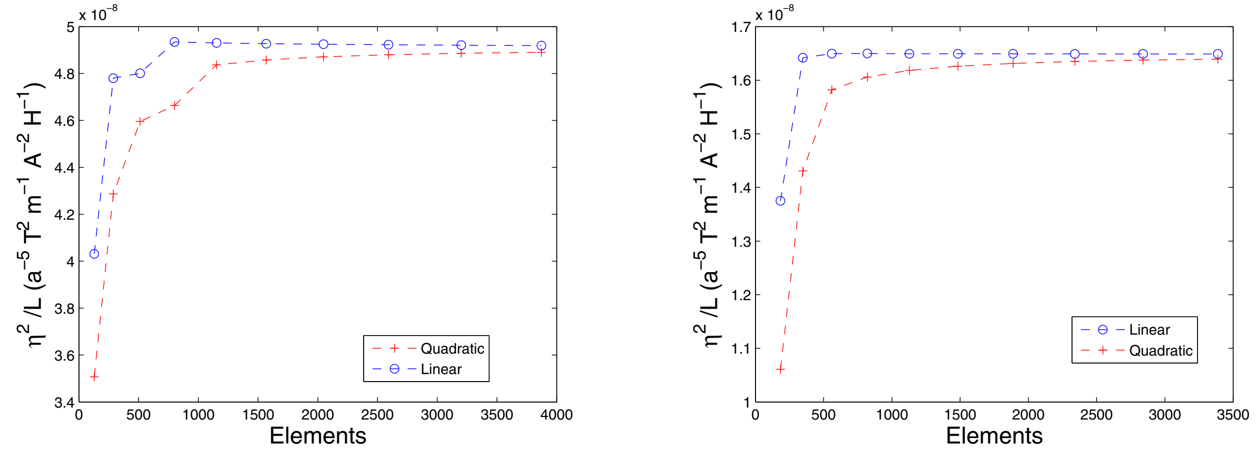

(a) (b)

Figure 11: The parameter η^2/L corresponding to (a) the cylindrical x−gradient coil, and (b) the hemispherical z−gradient coil, obtained using the optimal regularization parameter λ_{opt} chosen according to Eq. (52) and L = 351 internal points in the region of interest, as a function of the number of linear $(-\circ-)$ and quadratic $(-+-)$ triangular boundary elements.

boundary elements, the parameter η^2/L tends to a constant value as the number of elements used for discretising the coil surface, Γ_{coil}, increases. Hence we can conclude that the convergence of the proposed numerical method with respect to refining the BEM mesh size is also proven by considering the parameter η^2/L characterising the performance of gradient coils, for both coil geometries investigated.

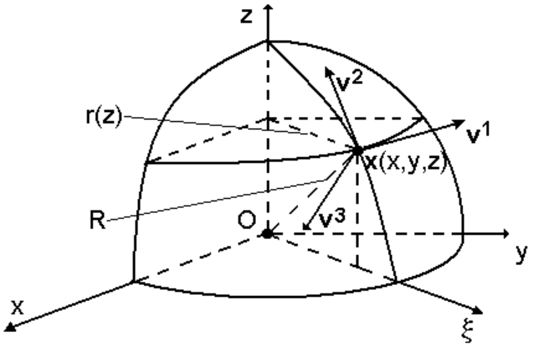

Figure 12: Quadratic triangular boundary element: Local spherical coordinate system.

6 Conclusions

In this paper, we have investigated the design of cylindrical and hemispherical gradient coils for MRI by considering the reconstruction of a divergence-free surface current distribution from knowledge of the magnetic flux density in a prescribed region of interest. This inverse problem was formulated in the framework of static electromagnetism using its corresponding integral representation according to potential theory. A novel quadratic BEM (i.e. linear interpolation) which satisfies the divergence-free condition for the current density was also proposed. In order to retrieve an accurate and physically correct numerical solution of this problem, a minimisation problem for the Tikhonov functional was solved. The latter was obtained by regularizing the least-squares functional, which measures the difference between the desired and numerically calculated magnetic fluxes in a region of interest, with respect to the norm induced by the magnetic energy. The numerically retrieved solutions of the inverse problem analysed in this paper were presented in terms of the contours of the stream function. The numerical results obtained for cylindrical and hemispherical x− and z−gradient coil designs using linear and quadratic boundary elements (i.e. constant and linear approximations) have showed the efficiency of the proposed numerical method, as well as an improvement in the accuracy in the case of quadratic elements.

References

Adriaens, J.P.; Delincé, F.; Dular, P.; Genon, A.; Legros, W.; Nicolet, A. (1991): Vector potential boundary element for three dimensional magnetostatics. *IEEE Transactions on Magnetics*, vol. 27, pp. 3808–3810.

Andersen, L.S.; Volakis, J.L. (1999): Development and applications of a novel class of hierarchical tangential vector finite elements for electromagnetics. *IEEE Transactions on Antennas and Propagation*, vol. 47, pp. 112–120.

Bangert, V.; Mansfield, P. (1982): Magnetic field gradient coils for NMR imaging. *Journal of Physics E: Scientific Instruments*, vol. 15, pp. 235–239.

Bowtell, R.W.; Mansfield, P. (1989): Minimum power flat gradient pairs for NMR microscopy. *Eighth Annual Meeting of the Society of Magnetic Resonance in Medicine*, pp. 977.

Brebbia, C.A.; Telles, J.F.C.; Wrobel, L.C. (1984): *Boundary Element Techniques*, Springer-Verlag, Berlin and New York.

Cai, W. (1999): High-order mixed current basis functions for electromagnetic scattering of curved surfaces. *Journal of Scientific Computing*, vol. 14, pp. 73–105.

Cai, W.; Yu, T.; Wang, H.; Yu, Y. (2001): High-order mixed RGW basis functions for electromagnetic applications. *IEEE Transactions on Microwave Theory and Techniques*, vol. 49, pp. 1295–1303.

Cai, W.; Yu, Y.; Yuan, X.C. (2002): Singularity treatment of high-order RGW basis functions for integral equations of electromagnetic scattering. *International Journal for Numerical Methods in Engineering*, vol. 14, pp. 73–105.

Carlson, C.W.; Derby, K.A.; Hawryszko, K.C.; Weideman, M. (1992): Design and evaluation of shielded gradient coils. *Magnetic Resonance in Medicine*, vol. 26, pp. 191–206.

Chao, R.-M.; Chen, Y.-J.; Lin, F.C. (2001): Determining the unknown traction of a cracked elastic body using the inverse technique with the dual boundary element method. *CMES: Computer Modeling in Engineering & Sciences*, vol. 2, pp. 73–86.

Green, D.; Bowtell, R.W.; Morris, P.G. (2002): Uniplanar gradient coil for brain imaging. *Tenth Annual Meeting of the International Society of Magnetic Resonance in Medicine*, Honolulu, Hawaii, USA.

Green, D.; Leggett, J.; Bowtell, R.W. (2005): Hemispherical gradient coils for magnetic resonance imaging. *Magnetic Resonance in Medicine*, vol. 54, pp. 656–668.

Hansen, P.C. (1998): *Rank-Deficient and Discrete Ill-Posed Problems: Numerical Aspects of Inversion*, SIAM, Philadelphia.

Jackson, J.D. (1998): *Classical Electrodynamics*, John Wiley & Sons, New York and London.

de Lacerda, L.A.; da Silva, J.M. (2006): A dual BEM genetic algorithm scheme for the identification of polarization curves of buried slender structures. *CMES: Computer Modeling in Engineering & Sciences*, vol. 14, pp. 153–160.

Leggett, J.; Crozier, S.; Blackband, S.; Bowtell, R.W. (2003): Multilayer transverse gradient coil design. *Concepts in Magnetic Resonance B: Magnetic Resonance Engineering*, vol. 16, pp. 38–46.

Lemdiasov, R.A.; Ludwig, R. (2005): A stream function method for gradient coil design. *Concepts in Magnetic Resonance B: Magnetic Resonance Engineering*, vol. 26B, pp. 67–80.

Lesnic, D.; Elliott, L.; Ingham, D.B. (1997): An iterative boundary element method for solving numerically the Cauchy problem for the Laplace equation. *Engineering Analysis with Boundary Elements*, vol. 20, pp. 123–133.

Lesnic, D.; Elliott, L.; Ingham, D.B. (1998): The solution of an inverse heat conduction problem subject to the specification of energies. *International Journal of Heat and Mass Transfer*, vol. 41, pp. 25–32.

Liu, H. (1998): Finite size bi-planar gradient coil for MRI. *IEEE Transactions on Magnetics*, vol. 34, pp. 2162–2164.

Marin, L.; Elliott, L.; Ingham, D.B.; Lesnic, D. (2001): Boundary element method for the Cauchy problem in linear elasticity. *Engineering Analysis with Boundary Elements*, vol. 25, pp. 783–793.

Marin, L.; Elliott, L.; Ingham, D.B.; Lesnic, D. (2002): Boundary element regularisation methods for solving the Cauchy problem in linear elasticity. *Inverse Problems in Engineering*, vol. 10, pp. 335–357.

Marin, L.; Elliott, L.; Heggs, P.J; Ingham, D.B.; Lesnic, D.; Wen, X. (2003): Conjugate gradient-boundary element solution to the Cauchy problem for Helmholtz-type equations. *Computational Mechanics*, vol. 31, pp. 367–377.

Marin, L.; Elliott, L.; Heggs, P.J; Ingham, D.B.; Lesnic, D.; Wen, X. (2004): Comparison of regularization methods for solving the Cauchy problem associated with the Helmholtz equation. *International Journal for Numerical Methods in Engineering*, vol. 60, pp. 1933–1947.

Martens, M.A.; Petropoulos, L.S.; Brown, R.W.; Andrews, J.H.; Morich, M.A.; Patrick, J.L. (1991): Insertable biplanar gradient coil for MR imaging. *Review of Scientific Instruments*, vol. 21, pp. 2639–2645.

Mustata, R.; Harris, S.D.; Elliott, L.; Lesnic, D.; Ingham, D.B. (2000): An inverse boundary element method for determining the hydraulic conductivity in anisotropic rocks. *CMES: Computer Modeling in Engineering & Sciences*, vol. 1, pp. 107–116.

Nedelec, J.C. (1980): Mixed finite elements in $\mathbb{R}^3$. *Numerische Mathematik*, vol. 35, pp. 315–341.

Nicolet, A. (1991): Modélisation du champ magnétique dans les systèmes comprenant des milieux non linéaires. *PhD Thesis*, University of Liège, Liège.

Nicolet, A. (1994): Boundary elements and singular integrals in 3D magnetostatics. *Engineering Analysis with Boundary Elements*, vol. 13, pp. 193–200.

Nicolet, A.; Dular, P.; Genon, A.; Legros, W. (1992): Boundary element singularities in 3D magnetostatics problems based on the vector potential. In: C.A. Brebbia & M.S. Ingber (eds.) *Boundary Element Technology VII*, Computational Mechanics Publications, Southampton and Boston, pp. 319–329.

Noroozi, S.; Sewell, P.; Vinney, J. (2006): The application of a hybrid inverse boundary element problem engine for the solution of potential problems. *CMES: Computer Modeling in Engineering & Sciences*, vol. 14, pp. 171–180.

Popovic, B.D.; Kolundzija, B.M. (1994): *Analysis of Metallic Antennas and Scatters*, IEE Press, UK.

Rao, S.M.; Wilton, D.R.; Glisson, A.W. (1982): Electromagnetic scattering by surfaces of arbitrary shape. *IEEE Transactions on Antennas and Propagation*, vol. AP-30, pp. 409–418.

Romeo, F.; Hoult, D.I. (1984): Magnet field profiling - Analysis and correcting coil design. *Magnetic Resonance in Medicine*, vol. 1, pp. 44–65.

Schweikert, K.H.; Krieg, R.; Noack, F. (1988): A high-field air-cored magnet coil design for fast-field-cycled NMR. *Journal of Magnetic Resonance*, vol. 78, pp. 77-96.

Tiknonov, A.N.; Arsenin, V.Y. (1986): *Methods for Solving Ill-Posed Problems*, Nauka, Moscow.

Turner, R. (1986): A target field approach to optimal coil desing. *Journal of Physics D: Applied Physics*, vol. 19, pp. L147–L151.

Turner, R. (1988): Minimum inductance coils. *Journal of Physics E: Scientific Instruments*, vol. 21, pp. 948–952.

Turner, R. (1993): Gradient coil design: A review of methods. *Magnetic Resonance Imaging*, vol. 11, pp. 903–920.

Wandzura, S. (1992): Electric current basis functions for curved surfaces. *Electromagnetics*, vol. 12, pp. 77–91.

Webb, J.P. (1993): Edge elements and what they can do for you. *IEEE Transactions on Magnetism*, vol. 29, pp. 275-281.

Wong, E.; Jesmanowicz, A.; Hyde, J.S. (1991): Coil optimization for MRI by conjugate gradient descent. *Magnetic Resonance in Medicine*, vol. 21, pp. 39–48.

Zeb, A.; Elliott, L.; Ingham, D.B.; Lesnic, D. (2000): Boundary element two-dimesional solution of an inverse Stokes problem. *Engineering Analysis with Boundary Elements*, vol. 24, pp. 75–88.

Zeb, A.; Elliott, L.; Ingham, D.B.; Lesnic, D. (2002): An inverse Stokes problem using interior pressure data. *Engineering Analysis with Boundary Elements*, vol. 26, pp. 739–745.

Appendix A: Shape functions and divergence-free basis functions for triangular boundary elements

For the sake of completeness, we list below the expressions for the shape functions, $\mathrm{N_j}$, and their derivatives, $\frac{\partial \mathrm{N_j}}{\partial \xi}$ and $\frac{\partial \mathrm{N_j}}{\partial \eta}$, the derivatives in the $\xi-$ and $\eta-$directions, $\tau^{\mathrm{n}\xi}$ and $\tau^{\mathrm{n}\eta}$, the surface metric, $\mathrm{J^n}$, and the basis vectors, $\mathbf{v}^{\mathrm{nj}}$, corresponding to the types of boundary element, Γ_{n}, used in this paper, see also Fig. 1. In the sequel, we use the following notation:

$$\zeta = \zeta(\xi,\eta) = 1 - \xi - \eta, \tag{58}$$

where $\xi, \eta \geq 0$, $\xi + \eta \leq 1$.

Linear triangular boundary elements ($\mathrm{N_e} = 3$)

Shape functions:

$$\mathrm{N}_1(\xi,\eta) = \xi \quad \mathrm{N}_2(\xi,\eta) = \eta \quad \mathrm{N}_3(\xi,\eta) = \zeta \tag{59}$$

Derivatives of the shape functions:

$$\begin{aligned}
\frac{\partial \mathrm{N}_1(\xi,\eta)}{\partial \xi} &= 1 & \frac{\partial \mathrm{N}_1(\xi,\eta)}{\partial \eta} &= 0 \\
\frac{\partial \mathrm{N}_2(\xi,\eta)}{\partial \xi} &= 0 & \frac{\partial \mathrm{N}_2(\xi,\eta)}{\partial \eta} &= 1 \\
\frac{\partial \mathrm{N}_3(\xi,\eta)}{\partial \xi} &= -1 & \frac{\partial \mathrm{N}_3(\xi,\eta)}{\partial \eta} &= -1
\end{aligned} \tag{60}$$

Derivatives in the $\xi-$ and $\eta-$directions:

$$\begin{aligned}
\tau^{\mathrm{n}\xi}(\xi,\eta) &= \mathbf{x}^{\mathrm{n}1} - \mathbf{x}^{\mathrm{n}3} = \tau^{\mathrm{n}\xi} \\
\tau^{\mathrm{n}\eta}(\xi,\eta) &= \mathbf{x}^{\mathrm{n}2} - \mathbf{x}^{\mathrm{n}3} = \tau^{\mathrm{n}\eta}
\end{aligned} \tag{61}$$

Surface metric (Jacobian):

$$\begin{aligned}
\mathrm{J^n}(\xi,\eta) &= |\tau^{\mathrm{n}\xi}(\xi,\eta) \times \tau^{\mathrm{n}\eta}(\xi,\eta)| \\
&= |\tau^{\mathrm{n}\xi} \times \tau^{\mathrm{n}\eta}| = \mathrm{J^n}
\end{aligned} \tag{62}$$

Vectors $\mathbf{v}^{\mathrm{ni}}(\xi,\eta)$:

$$\begin{aligned}
\mathbf{v}^{\mathrm{n}1}(\xi,\eta) &= \frac{\mathbf{x}^{\mathrm{n}3} - \mathbf{x}^{\mathrm{n}2}}{\mathrm{J^n}} = \mathbf{v}^{\mathrm{n}1} \\
\mathbf{v}^{\mathrm{n}2}(\xi,\eta) &= \frac{\mathbf{x}^{\mathrm{n}1} - \mathbf{x}^{\mathrm{n}3}}{\mathrm{J^n}} = \mathbf{v}^{\mathrm{n}2} \\
\mathbf{v}^{\mathrm{n}3}(\xi,\eta) &= \frac{\mathbf{x}^{\mathrm{n}2} - \mathbf{x}^{\mathrm{n}1}}{\mathrm{J^n}} = \mathbf{v}^{\mathrm{n}3}
\end{aligned} \tag{63}$$

Quadratic triangular boundary elements ($\mathrm{N_e} = 6$)

Shape functions:

$$\begin{aligned}
\mathrm{N}_1(\xi,\eta) &= \xi(2\xi - 1) & \mathrm{N}_4(\xi,\eta) &= 4\xi\eta \\
\mathrm{N}_2(\xi,\eta) &= \eta(2\eta - 1) & \mathrm{N}_5(\xi,\eta) &= 4\eta\zeta \\
\mathrm{N}_3(\xi,\eta) &= \zeta(2\zeta - 1) & \mathrm{N}_6(\xi,\eta) &= 4\zeta\xi
\end{aligned} \tag{64}$$

Derivatives of the shape functions:

$$
\begin{aligned}
\frac{\partial \mathrm{N}_1(\xi,\eta)}{\partial \xi} &= 4\xi - 1 & \frac{\partial \mathrm{N}_1(\xi,\eta)}{\partial \eta} &= 0 \\
\frac{\partial \mathrm{N}_2(\xi,\eta)}{\partial \xi} &= 0 & \frac{\partial \mathrm{N}_2(\xi,\eta)}{\partial \eta} &= 4\eta - 1 \\
\frac{\partial \mathrm{N}_3(\xi,\eta)}{\partial \xi} &= 1 - 4\zeta & \frac{\partial \mathrm{N}_3(\xi,\eta)}{\partial \eta} &= 1 - 4\zeta \\
\frac{\partial \mathrm{N}_4(\xi,\eta)}{\partial \xi} &= 4\eta & \frac{\partial \mathrm{N}_4(\xi,\eta)}{\partial \eta} &= 4\xi \\
\frac{\partial \mathrm{N}_5(\xi,\eta)}{\partial \xi} &= -4\eta & \frac{\partial \mathrm{N}_5(\xi,\eta)}{\partial \eta} &= 4(\zeta - \eta) \\
\frac{\partial \mathrm{N}_6(\xi,\eta)}{\partial \xi} &= 4(\zeta - \xi) & \frac{\partial \mathrm{N}_6(\xi,\eta)}{\partial \eta} &= -4\xi
\end{aligned}
\tag{65}
$$

Derivatives in the $\xi-$ and $\eta-$directions:

$$
\begin{aligned}
\tau^{\mathrm{n}\xi}(\xi,\eta) =& (4\xi-1)\mathbf{x}^{\mathrm{n}1} + (1-4\zeta)\mathbf{x}^{\mathrm{n}3} \\
& + 4\eta\mathbf{x}^{\mathrm{n}4} - 4\eta\mathbf{x}^{\mathrm{n}5} + 4(\zeta-\xi)\mathbf{x}^{\mathrm{n}6} \\
\tau^{\mathrm{n}\eta}(\xi,\eta) =& (4\eta-1)\mathbf{x}^{\mathrm{n}2} + (1-4\zeta)\mathbf{x}^{\mathrm{n}3} \\
& + 4\xi\mathbf{x}^{\mathrm{n}4} + 4(\zeta-\eta)\mathbf{x}^{\mathrm{n}5} - 4\xi\mathbf{x}^{\mathrm{n}6}
\end{aligned}
\tag{66}
$$

Surface metric (Jacobian):

$$\mathrm{J}^{\mathrm{n}}(\xi,\eta) = |\tau^{\mathrm{n}\xi}(\xi,\eta) \times \tau^{\mathrm{n}\eta}(\xi,\eta)| \tag{67}$$

Vectors $\mathbf{v}^{\mathrm{n}i}(\xi,\eta)$:

$$
\begin{aligned}
\mathbf{v}^{\mathrm{n}1}(\xi,\eta) =& \frac{1}{\mathrm{J}^{\mathrm{n}}(\xi,\eta)} \big[(1-4\eta)\mathbf{x}^{\mathrm{n}2} + (4\zeta-1)\mathbf{x}^{\mathrm{n}3} \\
& - 4\xi\mathbf{x}^{\mathrm{n}4} + 4(\eta-\zeta)\mathbf{x}^{\mathrm{n}5} + 4\xi\mathbf{x}^{\mathrm{n}6}\big] \\
\mathbf{v}^{\mathrm{n}2}(\xi,\eta) =& \frac{1}{\mathrm{J}^{\mathrm{n}}(\xi,\eta)} \big[(4\xi-1)\mathbf{x}^{\mathrm{n}1} + (1-4\zeta)\mathbf{x}^{\mathrm{n}3} \\
& + 4\eta\mathbf{x}^{\mathrm{n}4} - 4\eta\mathbf{x}^{\mathrm{n}5} + 4(\zeta-\xi)\mathbf{x}^{\mathrm{n}6}\big] \\
\mathbf{v}^{\mathrm{n}3}(\xi,\eta) =& \frac{1}{\mathrm{J}^{\mathrm{n}}(\xi,\eta)} \big[(1-4\xi)\mathbf{x}^{\mathrm{n}1} + (4\eta-1)\mathbf{x}^{\mathrm{n}2} \\
& + 4(\xi-\eta)\mathbf{x}^{\mathrm{n}4} + 4\zeta\mathbf{x}^{\mathrm{n}5} - 4\zeta\mathbf{x}^{\mathrm{n}6}\big]
\end{aligned}
\tag{68}
$$

Appendix B: Quadratic triangular boundary elements: Local spherical coordinate system

We first assume that two of the edges of the quadratic triangular boundary element under investigation are given by constant azimuthal, $\theta = \theta_0$, and colatitude spherical coordinates, $\phi = \phi_0$, where $\theta_0 \in [0,2\pi)$ and $\phi_0 \in [0,\pi]$, see also Fig. 12.

The curve $\phi = \phi_0$ can be parameterised as

$$\mathrm{x}^2 + \mathrm{y}^2 = \mathrm{r}(\mathrm{z})^2, \qquad \mathrm{z}^2 + \mathrm{r}(\mathrm{z})^2 = \mathrm{R}^2, \tag{69}$$

whilst the unit tangent vector, $\mathbf{v}^1(\mathbf{x})$, at this curve is given by

$$\mathbf{v}^1(\mathbf{x}) = -\frac{\mathrm{y}}{\mathrm{r}(\mathrm{z})}\mathbf{e}_{\mathrm{x}} + \frac{\mathrm{x}}{\mathrm{r}(\mathrm{z})}\mathbf{e}_{\mathrm{y}} \tag{70}$$

and hence we obtain

$$\nabla \cdot \mathbf{v}^1(\mathbf{x}) = 0. \tag{71}$$

Moreover, the curve $\theta = \theta_0$ can be parameterised as

$$
\begin{aligned}
& \xi : \mathrm{y}(\xi) = \alpha \mathrm{x}(\xi), \quad \alpha \in \mathbb{R} \implies \\
& \xi^2 = \mathrm{x}(\xi)^2 + \mathrm{y}(\xi)^2 = \left(1+\alpha^2\right)\mathrm{x}(\xi)^2 \\
& \xi = \sqrt{1+\alpha^2}\,\mathrm{x}(\xi) \\
& \mathbf{e}_\xi = \frac{1}{\sqrt{1+\alpha^2}}\left(\alpha\mathbf{e}_{\mathrm{x}} + \mathbf{e}_{\mathrm{y}}\right).
\end{aligned}
\tag{72}
$$

Consequently, the unit tangent vector, $\mathbf{v}^2(\mathbf{x})$, at the curve $\theta = \theta_0$, is given by

$$
\begin{aligned}
\mathbf{v}^2(\mathbf{x}) &= \frac{\mathrm{z}}{\mathrm{R}}\mathbf{e}_\xi - \frac{\xi}{\mathrm{R}}\mathbf{e}_{\mathrm{z}} \\
&= \frac{\mathrm{z}}{\mathrm{R}\sqrt{1+\alpha^2}}\left(\alpha\mathbf{e}_{\mathrm{x}} + \mathbf{e}_{\mathrm{y}}\right) - \frac{\mathrm{x}\sqrt{1+\alpha^2}}{\mathrm{R}}\mathbf{e}_{\mathrm{z}}
\end{aligned}
\tag{73}
$$

and therefore it satisfies the following relation

$$\nabla \cdot \mathbf{v}^2(\mathbf{x}) = 0. \tag{74}$$

Since the unit tangent vector at the third edge of the quadratic triangular boundary element, $\mathbf{v}^3(\mathbf{x})$, is defined as a linear combination of the unit tangent vectors $\mathbf{v}^1(\mathbf{x})$ and $\mathbf{v}^2(\mathbf{x})$, it follows that

$$\nabla \cdot \mathbf{v}^3(\mathbf{x}) = 0. \tag{75}$$

Therefore, on using the interpolation proposed for the surface current density, $\mathbf{J}^{\mathrm{coil}}$, in Section 3.3, as well as Eqs. (71), (74) and (75), we obtain the divergence-free property of the approximated surface current density, namely

$$\nabla \cdot \mathbf{J}^{\mathrm{coil}}(\mathbf{x}) = 0. \tag{76}$$

The above property can easily be shown to hold also in the general case by considering the rotation of a circle on a spherical surface into a circle on the same surface defined by either constant azimuthal, $\theta = \theta_0$, or constant colatitude spherical coordinates, $\phi = \phi_0$.